

Dynamics of an oscillatory boundary layer over a sediment bed in Euler-Lagrange simulations

Jonathan S. Van Doren and M. Houssem Kasbaoui 100

¹School for Engineering of Matter, Transport and Energy, Arizona State University, Tempe, AZ 85281, USA

Corresponding author: M. Houssem Kasbaoui, houssem.kasbaoui@asu.edu

(Received 16 April 2024; revised 2 September 2025; accepted 25 September 2025)

We investigate the dynamics of an oscillatory boundary layer developing over a bed of collisional and freely evolving sediment grains. We perform Euler-Lagrange simulations at Reynolds numbers $Re_{\delta} = 200$, 400 and 800, density ratio $\rho_p/\rho_f = 2.65$, Galileo number Ga = 51.9, maximum Shields numbers from 5.60×10^{-2} to 2.43×10^{-1} , based on smooth wall configuration, and Keulegan-Carpenter number from 134.5 to 538.0. We show that the dynamics of the oscillatory boundary layer and sediment bed are strongly coupled due to two mechanisms: (i) bed permeability, which leads to flow penetration deep inside the sediment layer, a slip velocity at the bed-fluid interface, and the expansion of the boundary layer, and (ii) particle motion, which leads to rolling-grain ripples at $Re_{\delta} = 400$ and $Re_{\delta} = 800$. While at $Re_{\delta} = 200$ the sediment bed remains static during the entire cycle, the permeability of the bed-fluid interface causes a thickening of the boundary layer. With increasing Re_{δ} , the particles become mobile, which leads to rolling-grain ripples at Re_{δ} = 400 and suspended sediment at $Re_{\delta} = 800$. Due to their feedback force on the fluid, the mobile sediment particles cause greater velocity fluctuations in the fluid. Flow penetration causes a progressive alteration of the fluid velocity gradient near the bed interface, which reduces the Shields number based upon bed shear stress.

Key words: boundary layer structure, sediment transport, particle/fluid flows

1. Introduction

In shallow areas of the ocean, the seafloor may be subject to large oscillating pressure gradients and strong shear forces. This causes sediment to become suspended and transported to new locations, where it is deposited as the shear force oscillates. A model flow often used to investigate this process is the oscillatory boundary layer (OBL) problem.

Stokes (1855) was amongst the first to address this problem, specifically in the limit where viscous effects dominate and where the bottom surface is represented as a smooth flat wall. Under these assumptions, Stokes (1855) derived analytical solutions that show the establishment of a boundary layer with characteristic thickness $\delta = \sqrt{2\nu/\omega}$, where ν is the fluid kinematic viscosity, and ω is the angular frequency of the oscillations. Due to the assumption of dominating viscous effects, these solutions apply only in the limit of very small Reynolds numbers $Re_{\delta} = U_0 \delta / \nu$, where U_0 is the velocity amplitude of the oscillations. Later, many researchers investigated the dynamics of OBLs over smooth and rough walls at larger Reynolds numbers, including when the Reynolds number is sufficiently high for turbulence to emerge (Hino, Sawamoto & Takasu 1976; Akhavan et al. 1991b; Sarpkaya 1993; Vittori & Verzicco 1998; Costamagna, Vittori & Blondeaux 2003; Salon, Armenio & Crise 2007; Carstensen et al. 2010, 2012; Pedocchi, Cantero & García 2011; Ozdemir, Hsu & Balachandar 2014; Ghodke & Apte 2016, 2018; Mazzuoli et al. 2016, 2020; Mazzuoli & Vittori 2019; Vittori et al. 2020; Fytanidis, García & Fischer 2021). However, it is unclear whether these results are applicable to seafloors. Unlike the previously studied configurations with impermeable and fixed smooth or rough walls, seafloors are made of sediment particles that together form a porous bed. Depending on the details of the flow over it, the bed may be static, with or without bedforms, and may even evolve dynamically as sediment particles saltate or become suspended by the flow (Finn, Li & Apte 2016). In this paper, we investigate how the dynamics of an OBL couple with those of a bottom collisional and freely evolving sediment bed at increasingly large Reynolds numbers.

There has been significant effort devoted to the characterisation of the boundary layer that develops over a smooth or rough wall under the action of an oscillatory forcing. Depending on the Reynolds number Re_{δ} , different regimes have been identified (as detailed in Akhavan et al. 1991a; Vittori & Verzicco 1998; Pedocchi et al. 2011; Ozdemir et al. 2014; Fytanidis et al. 2021). To summarise, an OBL developing over an impermeable wall may exhibit four different regimes. The laminar regime occurs in smooth, rough and wavy wall OBLs at $Re_{\delta} \lesssim 85$. In this regime, the flow is laminar throughout the oscillation cycle (Blondeaux & Seminara 1979; Akhavan et al. 1991a; Vittori & Verzicco 1998), and is well described by the analytical solutions of Stokes (1855). For $85 \lesssim Re_{\delta} \lesssim 550$, the flow is in the disturbed laminar regime (Hino et al. 1976; Jensen, Sumer & Fredsøe 1989). The latter is characterised by the appearance of small-amplitude perturbations superimposed upon the Stokes flow (Vittori & Verzicco 1998). Fytanidis et al. (2021) found that the Reynolds number thresholds for this regime depend strongly on background disturbances. For $550 \lesssim Re_{\delta} \lesssim 3460$, the flow enters the intermittent turbulent regime, and is characterised by sudden turbulence eruption during the decelerating portion of the oscillatory period before relaminarising again. Finally, the turbulent regime occurs for $Re_{\delta} \gtrsim 3460$. In this regime, Jensen *et al.* (1989) show that the OBL presents sustained velocity fluctuations and a logarithmic layer for at least 90 % of the cycle.

Note that with a bottom rough wall, the Reynolds number thresholds between the different regimes may vary considerably, as the flow characteristics depend on additional roughness parameters, such as the Keulegan–Carpenter number $KC = U_0/(\omega d_p)$, where d_p represents the roughness size. Jensen *et al.* (1989) showed that disturbances caused by fixed sandpaper roughness lead to a thicker boundary layer and increased turbulence intensity. Similarly, Xiong *et al.* (2020) found that a flow disturbance created by a wall-mounted obstacle leads to earlier transition to turbulence, thereby lowering the threshold Re_δ compared to that found for a smooth wall OBL. Additional studies of roughness effects can be found in Ghodke & Apte (2016, 2018) and Mazzuoli & Vittori (2019).

Permeability may also have a significant effect on the structure of an OBL developing over a particle bed. Conley & Inman (1994) performed experiments with a ventilated OBL, i.e. an OBL with periodic transpiration over a permeable wall. They found that the wall shear stress decreases during suction and increases during injection. For a permeable wall, the no-slip condition may no longer hold, as observed by Liu, Davis & Downing (1996) and Breugem, Boersma & Uittenbogaard (2006). By comparing simulations of an OBL with experimental data, Meza-Valle & Pujara (2022) showed that a mixed boundary condition at the surface best captures the flow over a permeable wall. A permeable bed allows flow penetration, which in turn creates a Kelvin–Helmholtz instability and an inflection point in the fluid velocity within the boundary layer (Sparrow *et al.* 2012; Voermans, Ghisalberti & Ivey 2017). All these modifications caused by the bed permeability make it difficult to estimate the bed shear stress beforehand (Yuan & Madsen 2014).

The studies discussed thus far considered fixed porous beds. In the case of mobile beds, particle transport may further alter the bed-fluid interface. Particle motion leads to the emergence of new regimes, as discussed by Finn & Li (2016), who proposed a regime map for sediment-turbulent interactions. In the no-motion regime, the bed remains stationary and acts as previously described. In the bedform regime, ripples emerge in the particle bed as particles saltate over the surface. The study of Mazzuoli, Kidanemariam & Uhlmann (2019), by means of particle-resolved direct numerical simulations (PR-DNS), illustrates this regime. The authors showed the emergence of rolling-grain ripples in an OBL developing over a sediment bed at $Re_{\delta} \sim 100$, density ratio $\rho_p/\rho_f \sim 2.5$, and Galileo number $Ga \sim 10$. The latter represents the relative effect of gravitational and viscous forces exerted on sediment grains. An earlier study showed that ripples emerge from the interaction between particle rows and recirculation zones in the OBL (Mazzuoli et al. 2016). In the sheet flow regime, the bed-fluid interface recedes due to the formation of a layer of suspended particles (Hsu, Jenkins & Liu 2004; O'Donoghue & Wright 2004). Mazzuoli et al. (2020) showed that the eruption of turbulence plays a role in the sediment resuspension. Further, at relatively low values of the Shields number, sediment transport may depend on both Shields number and flow acceleration.

Several computational methods can be leveraged to study the dynamics of an OBL over a sediment bed. The PR-DNS, in which the boundary layer around each sediment grain is fully resolved, provides the highest fidelity since it requires little to no modelling (Uhlmann 2005; Apte, Martin & Patankar 2009; Breugem 2012; Kempe & Fröhlich 2012; Kasbaoui & Herrmann 2025). However, this results in very high computational cost, as seen from the PR-DNS of Mazzuoli et al. (2019). While using smaller computational domains and shorter integration times may reduce computational cost, it also introduces numerical artefacts. For example, the domain considered in the PR-DNS of Mazzuoli et al. (2020) was too small to allow the natural formation of ripples in the sediment bed. Even with this restrictive domain size, the high cost of the PR-DNS of Mazzuoli et al. (2020) limited the integration time to the first 1-4 cycles of the OBL, which may not be enough to reach a statistically quasi-periodic state. In contrast, the Euler-Lagrange method provides a good balance between computational cost and fidelity (Capecelatro & Desjardins 2013a; Finn et al. 2016). In this approach, flow features and bed dynamics on scales larger than the particle size are well resolved, while the flow on the scale of the particle is modelled. This makes it possible to simulate the dynamics on length and time scales much larger than those accessible in PR-DNS. Earlier studies showed that this approach can reproduce with high fidelity the dynamics of dense fluidised beds (Capecelatro & Desjardins 2013a) and dense slurries (Capecelatro & Desjardins 2013b; Arolla & Desjardins 2015), including in sheet flow and bedform regimes. More recently, Rao & Capecelatro (2019) showed that predictions with the Euler-Lagrange method for the evolution of sediment bed under both laminar and turbulent shear flow match very well with PR-DNS (Kidanemariam & Uhlmann 2014) and experiments (Aussillous *et al.* 2013).

In this paper, we study the interplay between an OBL and a sediment bed made of collisional and freely evolving particles from the laminar regime to the onset of turbulence using Euler-Lagrange simulations. The structure of the paper is as follows. In § 2, we provide the governing equations that dictate the evolution of the flow and sediment particles. In § 3, we provide details on the computations and parameters used in this study. Next, we analyse statistics of the fluid and solid phases in § 4, highlighting how sediment bed dynamics couple with those of the OBL. Finally, we give concluding remarks in § 5.

2. Governing equations

We use the volume-filtering approach of Anderson & Jackson (1967) and the Euler–Lagrange methodology of Capecelatro & Desjardins (2013a) to describe the dynamics of the sediment-laden flow. The carrier phase is an incompressible fluid with density ρ_f and viscosity μ_f . The volume-filtered Navier–Stokes equations read

$$\frac{\partial}{\partial t}(\alpha_f \rho_f) + \nabla \cdot (\alpha_f \rho_f \mathbf{u}_f) = 0, \tag{2.1}$$

$$\frac{\partial}{\partial t}(\alpha_f \rho_f \mathbf{u}_f) + \nabla \cdot (\alpha_f \rho_f \mathbf{u}_f \mathbf{u}_f) = \nabla \cdot (\mathbf{\tau} + \mathbf{R}_{\mu}) + \alpha_f \rho_f \mathbf{g} - \mathbf{F}_p + \mathbf{A}, \tag{2.2}$$

where α_f is the fluid volume fraction, u_f is the volume-filtered fluid velocity, $\tau = -pI + \mu[\nabla u_f + \nabla u_f^{\rm T} - (2/3)(\nabla \cdot u_f)I]$ is the resolved fluid stress tensor (Capecelatro & Desjardins 2013a), p is pressure, which includes the hydrostatic contribution, g is the gravitational acceleration, and F_p is the momentum exchange between the particles and the fluid. The tensor R_μ represents the so-called residual viscous stress tensor. This term arises from filtering the pointwise stress tensor. It includes sub-filter scale terms that require closure. This term is believed to be responsible for the apparent enhanced viscosity observed in viscous fluids containing suspended solid particles. For this reason, Capecelatro & Desjardins (2013a) proposed a closure using an effective viscosity, which, when combined with the effective viscosity model of Gibilaro $et\ al.\ (2007)$, leads to an expression for the residual viscous stress tensor:

$$\mathbf{R}_{\mu} = \mu_f (\alpha_f^{-2.8} - 1) \left[\nabla \mathbf{u}_f + \nabla \mathbf{u}_f^{\mathrm{T}} - \frac{2}{3} (\nabla \cdot \mathbf{u}_f) \mathbf{I} \right]. \tag{2.3}$$

We do not use an eddy viscosity model since none of the cases that we discuss here leads to fully developed turbulence.

In order to study the dynamics of an OBL, we drive the flow using the last term in (2.2), expressed as

$$A = \alpha_f \rho_f U_0 \omega \cos(\omega t) \, \boldsymbol{e}_x. \tag{2.4}$$

This represents a harmonic pressure gradient forcing with angular frequency ω and velocity amplitude U_0 . Here, x is the coordinate in the streamwise direction along the unitary vector \mathbf{e}_x , y is the coordinate in the wall-normal direction, and z is the coordinate in the spanwise direction.

The particles are described in the Lagrangian frame. Following Maxey & Riley (1983), the equations of motion of a particle i are given by

$$\frac{\mathrm{d}x_p^i}{\mathrm{d}t}(t) = u_p^i(t),\tag{2.5}$$

$$m_p \frac{\mathrm{d} u_p^i}{\mathrm{d} t}(t) = f_p^{h,i} + f_p^{c,i},$$
 (2.6)

$$I_p \frac{\mathrm{d}\boldsymbol{\omega}_p^i}{\mathrm{d}t}(t) = \boldsymbol{T}_p^{c,i},\tag{2.7}$$

where x_p^i , u_p^i , ω_p^i , m_p and I_p are the particle position, velocity, angular velocity, mass and moment of inertia, respectively. Here, $f_p^{h,i}$ represents the hydrodynamic force, which is modelled as (Van Doren & Kasbaoui 2024)

$$f_p^{h,i}(t) = V_p \nabla \cdot \tau|_{\mathbf{x}_p^i} + m_p f_d \frac{\mathbf{u}_f(\mathbf{x}_p^i, t) - \mathbf{u}_p^i}{\tau_p} + f_p^{am,i} + f_p^{lift,i},$$
(2.8)

where $V_p = \pi d_p^3/6$ is the particle volume. The first term on the right-hand side of (2.8) represents the effect of the undisturbed flow field (Maxey & Riley 1983). The second term represents the drag force exerted on a particle. Note that $\tau_p = \rho_p d_p^2/(18\mu)$ is the particle response time, and f_d is a drag correction factor. We use the one by Tenneti, Garg & Subramaniam (2011), derived from PR-DNS, which accounts for both inertial and high particle volume fraction effects. The last two terms on the right-hand side of (2.8) represent the added mass and Saffman lift (Saffman 1965) forces,

$$f_p^{am,i} = \frac{1}{2} \alpha_f \rho_f V_p \left(\frac{\mathrm{D} \boldsymbol{u}_f(\boldsymbol{x}_p^i, t)}{\mathrm{D}t} - \frac{\mathrm{d} \boldsymbol{u}_p^i}{\mathrm{d}t} \right), \tag{2.9}$$

$$\boldsymbol{f}_{p}^{lift,i} = 1.615 J \mu_{f} d_{p} |\boldsymbol{u}_{s}^{i}| \sqrt{\frac{d_{p}^{2} |\boldsymbol{\omega}^{i}| \alpha_{f} \rho_{f}}{\mu_{f}}} \frac{\boldsymbol{u}_{s}^{i} \times \boldsymbol{\omega}^{i}}{|\boldsymbol{u}_{s}^{i}| |\boldsymbol{\omega}^{i}|}, \tag{2.10}$$

where $\omega^i = \omega_f(x_p^i, t)$ is the fluid vorticity at the particle location, $u_s^i = u_f(x_p^i, t) - u_p^i$ is the slip velocity, and J is a lift correction, which is equal to 1 in the model from Saffman (1965).

The term $f_p^{c,i}$ represents the collisional force exerted on the particle due to particle—particle and particle—wall collisions. These collisions are modelled using the soft-sphere model, as detailed in Capecelatro & Desjardins (2013a). Briefly, the force exerted on particle a due to a collision with particle b, denoted $f_p^{c,b\to a}$, is decomposed into normal and tangential components. The normal component $f_{p,n}^{c,b\to a}$ is modelled as a linearised spring—dashpot system, i.e.

$$f_{p,n}^{c,b\to a} = \begin{cases} -k\delta_{ab}\mathbf{n}_{ab} - \eta\mathbf{u}_{ab,n} & \text{if } \left|\mathbf{x}_p^a - \mathbf{x}_p^b\right| < 0.5\left(d_p^a + d_p^b\right) + \lambda, \\ 0 & \text{otherwise,} \end{cases}$$
(2.11)

where $\delta_{ab} = 0.5(d_p^a + d_p^b) - |\mathbf{x}_p^a - \mathbf{x}_p^b|$ is the overlap between particles a and b, \mathbf{n}_{ab} is the unit normal vector between the particles, and $\mathbf{u}_{ab,n}$ is the normal relative velocity. The parameters k and the η are the spring stiffness and damping factor, respectively.

Note that the governing equations (2.1) and (2.2) for the fluid phase are solved in both simulations with particles and without. In the latter case, $\alpha_f = 1$ throughout the domain, which recovers the standard Navier–Stokes equations.

The solid phase dynamics is coupled with the fluid phase dynamics through the momentum exchange field \mathbf{F}_p , and the volume fraction fields, α_f and α_p . We calculate these fields using

Cases	Re_{δ}	$ ho_p/ ho_f$	Ga	KC	d_p/δ	θ_{max}
1	200	2.65	51.9	134.5	0.7435	5.60×10^{-2}
2	400	2.65	51.9	269.0	0.7435	1.12×10^{-1}
3	800	2.65	51.9	538.0	0.7435	2.43×10^{-1}

Table 1. Summary of the non-dimensional parameters for the present runs of an OBL over a sediment bed. The maximum Shields number is determined *a priori* from the smooth wall shear stress as described in § 4.2.

$$F_p(x,t) = \sum_{i=1}^{N} f_p^{h,i}(t) g(\|x - x_p^i\|), \qquad (2.12)$$

$$\alpha_p(\mathbf{x}, t) = \sum_{i=1}^{N} V_p g(\|\mathbf{x} - \mathbf{x}_p^i\|), \qquad (2.13)$$

$$\alpha_f(\mathbf{x}, t) = 1 - \alpha_p(\mathbf{x}, t). \tag{2.14}$$

In these equations, g represents a Gaussian filter with width $\delta_f = 5d_p$. We study the influence of filter width on fluid statistics in Appendix A, and show that the statistics are converged with respect to filter width at $\delta_f = 5d_p$. Additional details on the computation of these terms and validation of the computational strategy, can be found in Capecelatro & Desjardins (2013a,b), Capecelatro, Pepiot & Desjardins (2014) and Rao & Capecelatro (2019), and in our recent work (Kasbaoui 2019; Kasbaoui, Koch & Desjardins 2019; Shuai & Kasbaoui 2022; Shuai $et\ al.\ 2022$; Dave & Kasbaoui 2023; Shuai, Roy & Kasbaoui 2024; Van Doren & Kasbaoui 2024). In Appendix D, we further demonstrate the ability of this approach to capture sediment transport accurately. This is done by comparing sediment flow rates obtained with this method in laminar channel flows at varying Shields numbers with those obtained from PR-DNS (Kidanemariam & Uhlmann 2014) and laboratory experiments (Aussillous $et\ al.\ 2013$). Based on the excellent agreement shown in Appendix D, we conclude that this Euler–Lagrange method is well suited for this study.

3. Numerical experiments

3.1. Configuration

We consider the dynamics of an OBL over a cohesionless particle bed at three Reynolds numbers, $Re_{\delta} = 200$, 400 and 800. A summary of the relevant non-dimensional parameters for each run is given in table 1. In order to provide a baseline for comparisons with the sediment-laden cases, we also carry out companion simulations at the same Reynolds numbers but with a bottom smooth and impermeable wall instead of a particle bed (see Appendix A). Note that without the particle bed, the flow at $Re_{\delta} = 200$ and 400 is in the laminar regime (see Appendix A). We do not observe a disturbed laminar regime in these simulations due to the wall being smooth and flat, and the absence of any external disturbances. Without small pertubations, the disturbed laminar regime would take much longer to emerge than the simulations that we performed. The flow at $Re_{\delta} = 800$ falls in the intermittent turbulent regime. Comparing the simulations with and without a bottom particle bed helps to elucidate the impact of sediment motion, bedforms and bed permeability on the flow statistics.

In addition to the Reynolds number Re_{δ} , the presence of particles introduces additional dimensionless parameters. These are:

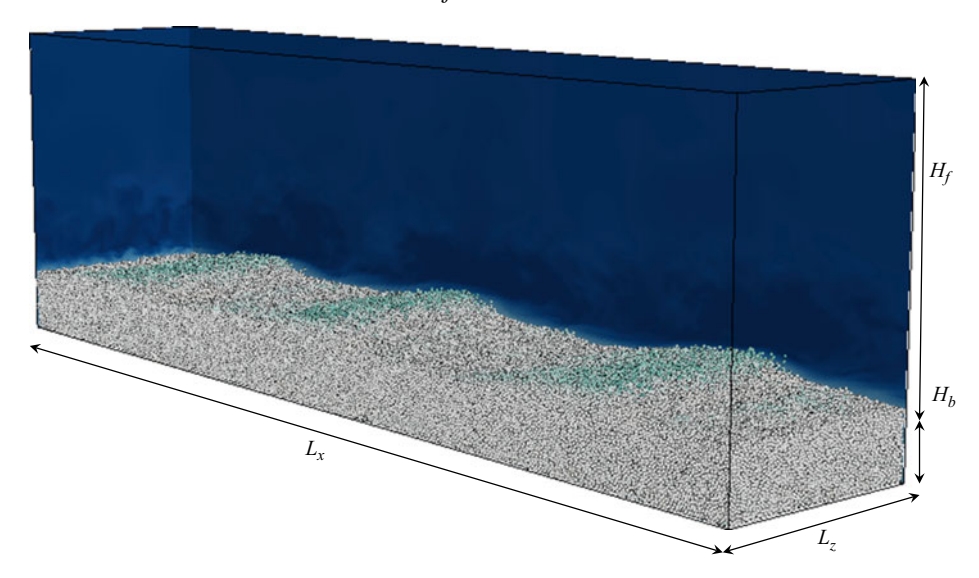


Figure 1. Schematic of the configuration with a bottom sediment bed. The latter is generated in precursor runs where the particles are seeded towards the middle of the domain and allowed to settle on the bottom boundary.

- (i) the density ratio ρ_p/ρ_f ,
- (ii) the Galileo number $Ga = d_p \sqrt{(\rho_p/\rho_f 1)gd_p}/v$,
- (iii) the Keulegan–Carpenter number $KC = U_0/\omega d_p$.

Although not an independent number, the Shields number $\theta_{max} = \tau_{b,max}/((\rho_p - \rho_f)gd_p)$, where $\tau_{b,max}$ is the maximum bed shear stress, is also an important non-dimensional number to consider. The values for each case are shown in table 1. From a dimensional perspective, these cases may correspond to an oscillating flow with period T = 1.75 s, velocity amplitude varying from $U_0 = 0.134$ m s⁻¹ to $U_0 = 0.536$ m s⁻¹, and sand particles with diameter 550 μ m.

Finn *et al.* (2016) suggest that the regimes of particle transport are determined by the combination of Shields numbers and Galileo numbers. Based on their work and the combination of the present parameters, case 1 ($Re_{\delta} = 200$) falls into the 'no-motion regime'. Cases 2 ($Re_{\delta} = 400$) and 3 ($Re_{\delta} = 800$) fall in the gravitational settling regime. We expect particle motion in both of these cases, with notably higher suspended sediment concentration in case 3 compared to case 2. In all these cases, the Keulegan–Carpenter number is very large, which suggests that inertial forces on particles caused by the unsteady flow oscillations are negligible compared to the drag force due to the instantaneous slip.

Figure 1 shows a schematic of the computational domain that we use for the present simulations. Table 2 gives a summary of the computational parameters. The domain has length 250δ in the streamwise direction, and 50δ in the spanwise direction. The domain height in the normal direction is $H_f + H_b$, where $H_f = 61.9\delta$ is the height of the clear fluid column, and $H_b = 16.7\delta$ is the initial bed height. We chose the latter sufficiently deep $(H_b \sim 22d_p)$ to accurately account for the flow intrusion within the bed. This gives a total number of particles $N = 6.09 \times 10^5$.

To discretise the governing equations, we use a uniform grid with spacing $\Delta x = d_p/2$, which provides a high resolution of the momentum coupling between particles and fluid. This results in a grid of size $672 \times 211 \times 134$. In Appendix C, we conduct a grid

Cases	N_{x}	N_y	N_z	L_x/δ	L_z/δ	H_f/δ	H_b/δ
With bed					50		
Without bed	64	256	64	50	25	40	0

Table 2. Summary of domain parameters.

convergence study and show that this discretisation is sufficient for $Re_{\delta} = 800$. The time step Δt is such that $\Delta t/T = 1.79 \times 10^{-5}$. This restrictive time step is imposed by the requirement in the soft-sphere collision model that the bottom layer of the particles must support the weight of the particle bed above it. This is satisfied by ensuring that the spring stiffness in the collision model is sufficiently large to maintain a realistic volume fraction 0.63 for a poured bed (Scott & Kilgour 1969; more details in Capecelatro & Desjardins 2013a). We use periodic boundary conditions in the streamwise and spanwise directions. In the wall-normal direction, we use far-field boundary conditions at the top, and a no-slip condition at the bottom. Note that the bottom layer of particles is held fixed, whereas all other particles are free to move according to the evolution equations (2.5)–(2.7). Following Charru *et al.* (2016), the particle restitution coefficient is maintained at 0.8, and the particle friction coefficient at 0.4. Note that Kidanemariam & Uhlmann (2014) showed that the precise value of the friction coefficient does not have a significant impact on sediment transport.

The protocol to initialise the simulations and gathering statistics is as follows. We perform precursor simulations to generate a realistic poured bed as described in § 3.2. Then we carry out simulations initialised from quiescent flow. We run the simulations for several periods until the flow reaches a periodic state and loses the effect of the initial conditions. This takes approximately two periods. After this, we run the simulations for additional eight periods to collect and compute phase-averaged statistics. We ensure that the statistics are converged by confirming that adding data from additional periods does not change the phase-averaged statistics.

While the computational cost of these Euler–Lagrange simulations is high, nevertheless they remain achievable with today's supercomputing resources. Each case requires approximately 400 000 CPU-hours on AMD EPYC 7742 CPUs. This is equivalent to approximately 15 days of run time on 1152 CPUs. The total cost is 1.2M CPU-hours for the three cases with sediment beds.

In contrast, the cost of doing PR-DNS of these cases largely exceeds computing resources afforded to most academic researchers, if not being completely intractable. Taking a typical discretisation of 16 grid points per diameter ($\Delta x = d_p/16$) (Kidanemariam & Uhlmann 2014; Mazzuoli *et al.* 2019; Kasbaoui & Herrmann 2025), PR-DNS require 512 times more grid points than an Euler–Lagrange simulation of the same case. Thus we estimate the computational cost to be 614.4M CPU-hours to complete all three cases. This puts the simulation run time at approximately 21 years per case on 1152 CPUs.

3.2. Bed formation and the bed-fluid interface

To form the sediment bed, we perform precursor simulations that serve to generate a realistic bed volume fraction that matches the volume fraction of a poured bed, approximately 63 % (Scott & Kilgour 1969). In these runs, the oscillatory forcing is turned off, and the particles are initially uniformly distributed towards the middle of the domain at average volume fraction 40 % and with small random velocity fluctuations. We then

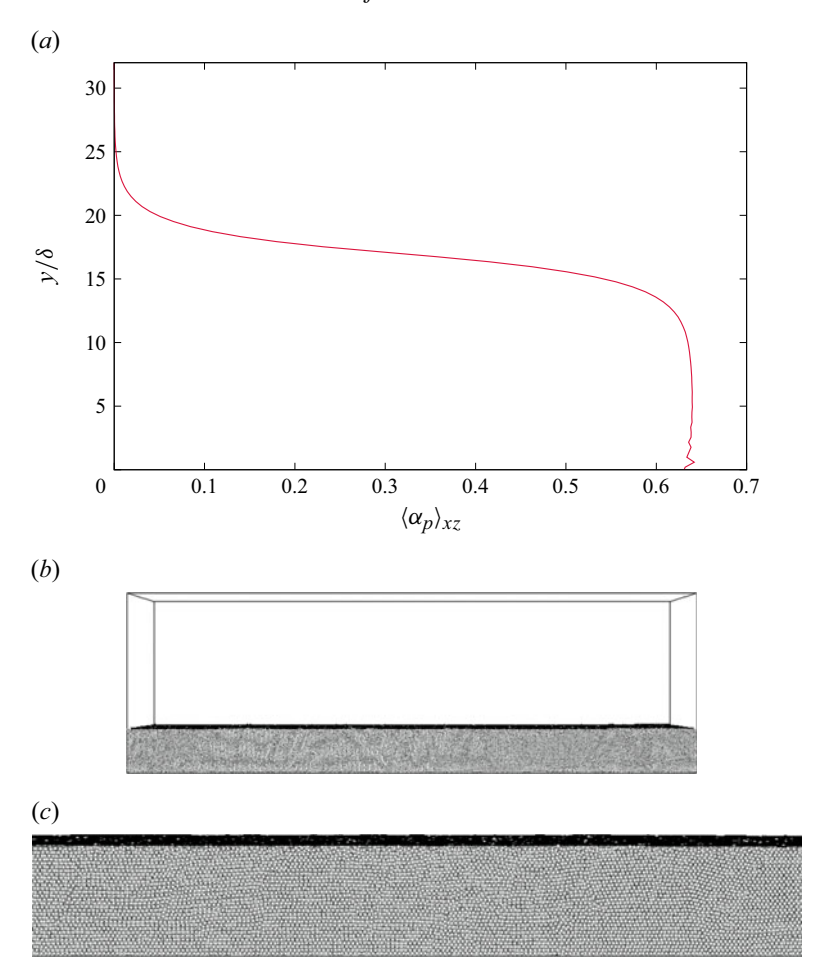


Figure 2. The particle bed is initialised by letting particles settle onto the bottom wall. (a) This procedure results in a volume fraction profile that is consistent with that of a poured bed. (b,c) The isosurface $\alpha_p = 0.2$ represents a good indicator of the location of the bed–fluid interface.

integrate the governing equations (2.1), (2.2), (2.5), (2.6) and (2.7) until the particles fully settle down. Particle–particle collisions and fluid-mediated particle–particle interactions lead to the formation of the poured bed in figure 1.

Figure 2(a) shows the average particle volume fraction $\langle \alpha_p \rangle_{xz}$ profile as a function of the wall-normal distance. Note that here and hereafter, the notation $\langle \cdot \rangle_{xz}$ refers to ensemble and spatial averaging over the streamwise (x) and spanwise (z) directions. As anticipated, the volume fraction within the bed matches the random poured packing (Scott & Kilgour 1969). It smoothly transitions to zero away from the bed. Further, we conduct the simulations with particle beds that are sufficiently deep to ensure that the interaction between the particle bed and the turbulent flow above is captured without interference from the bottom boundary. In the present study, the sediment bed has thickness approximately 22 particle diameters, which corresponds to $\sim 16.7\delta$.

At this point, we must address the way in which we define the bed-fluid interface. We follow the approach of Kidanemariam & Uhlmann (2014), and define the bed-fluid interface using an isosurface of the particle volume fraction $\alpha_p = \alpha_{p,b} < 0.63$. This is also similar to the experimental approach of Aussillous *et al.* (2013), where black/white

J.S. Van Doren and M.H. Kasbaoui

thresholding of side view frames of the bed are used to detect the bed interface. However, it is important to recognise that the choice of the isosurface $\alpha_{p,b}$ demarcating the bed-fluid interface is somewhat arbitrary since the computation of the volume fraction field α_p depends on numerical choices. For example, the shape and size of the filter kernel used to compute α_p control the width of the transition region in figure 2(a). With the filtering described in § 2, the isosurface $\alpha_{p,b} = 0.2$ provides a good indicator of the approximate location of the bed-fluid interface. We determine this by verifying that this surface lies right on top of the particles, as shown in figures 2(b,c).

4. Characteristics of an OBL over a cohesionless particle bed

Before proceeding further, we refer the reader to Appendix A for a review of the flow features observed when the OBL develops over a smooth and impermeable wall at $Re_{\delta} = 200$, 400 and 800. These characteristics provide a benchmark for comparison in what follows. Having reviewed these dynamics, we now analyse the changes that occur when the OBL develops over a cohesionless particle bed.

4.1. Overview of the dynamics

The presence of a sediment bed leads to notable flow disturbances, even at low Re_{δ} for which DNS of OBLs over smooth and impermeable walls show flow fields devoid of any fluctuations. At $Re_{\delta}=200$, small imperfections in the bed-fluid interface are responsible for flow disturbances. This is shown in figure 3, depicting the instantaneous spanwise vorticity in a wall-normal plane at different phases of the cycle. To highlight the bedform, figure 3 also shows the volume fraction contour $\alpha_p=\alpha_{p,b}=0.2$ that demarcates the sediment bed-fluid interface. The small imperfections in the bed-fluid interface are the result of the initial bed generation as described in § 3.2. At $Re_{\delta}=200$, the bed shear stress is too low to induce any significant motion of the particles. Thus the initial bedform persists throughout the simulation. The resulting flow fluctuations are reminiscent of the fluctuations described by Vittori & Verzicco (1998) in the disturbed laminar regime, where the bottom wall has small waviness. Since a smooth and impermeable wall does not generate such fluctuations at $Re_{\delta}=200$ (see Appendix A), this suggests that flow disturbances induced by asperities in the bed-fluid interface are the driving mechanics at this Reynolds number.

At $Re_{\delta} = 400$, the particles in the bed's top layers become mobile. This leads to a dynamically evolving bed-fluid interface and greater flow disturbances, as shown in figure 4. Flow disturbances are strongest around phases 90° and 120°, i.e. from the maximum fluid velocity, and into the decelerating portion of the period. The vortex structures observed at these phases show chaotic behaviour, whereby larger structures spin off and break down into smaller ones. However, the range of scales is limited compared to what may be expected for a fully turbulent flow. The bed-fluid interface, marked by the black line in figure 4, changes dynamically with phase. This is due to particles being transported in the top layers of the bed, which couples the bedform dynamics to that of the flow over it.

We also note that bed permeability is significant at $Re_{\delta} = 400$. Whereas the extent of the flow intrusion below the bed-fluid interface is of the order of one Stokes thickness δ at $Re_{\delta} = 200$, the vortices generated at $Re_{\delta} = 400$ penetrate down by up to 4δ , judging from figures 3 and 4. Owing to the bed permeability, these vortices push fluid into and out of the bed. This plays an important role in the dynamic evolution of the bed-fluid interface, as flow exiting the bed exerts an upward drag force on the particles that helps to suspend or set into motion particles in the bed's top layers (Jewel, Fujisawa & Murakami 2019).

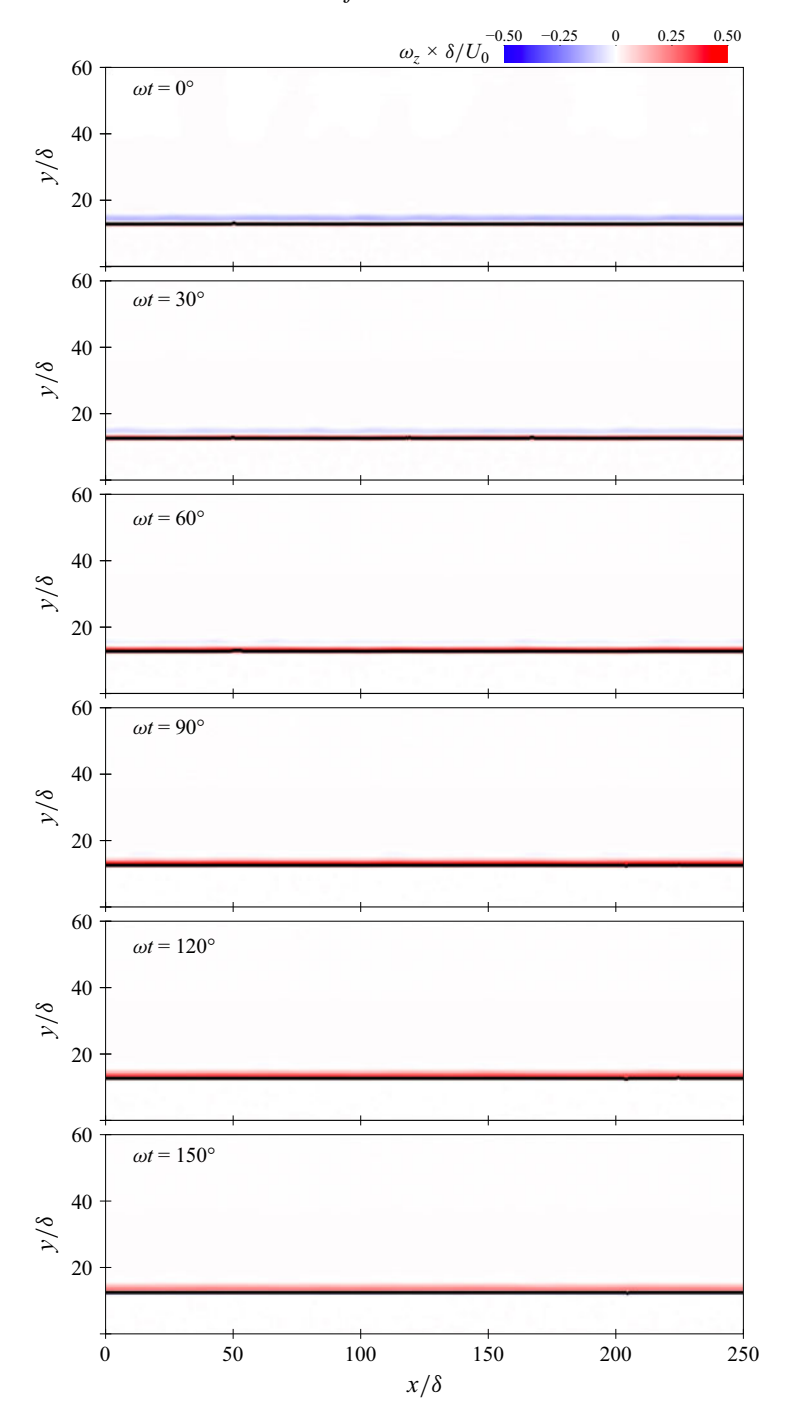


Figure 3. Zoomed-in views of the instantaneous spanwise vorticity and bed-fluid interface (solid line) at $Re_{\delta} = 200$. Small ripples in the bedform cause flow disturbances and fluctuations associated with the disturbed laminar regime.

J.S. Van Doren and M.H. Kasbaoui

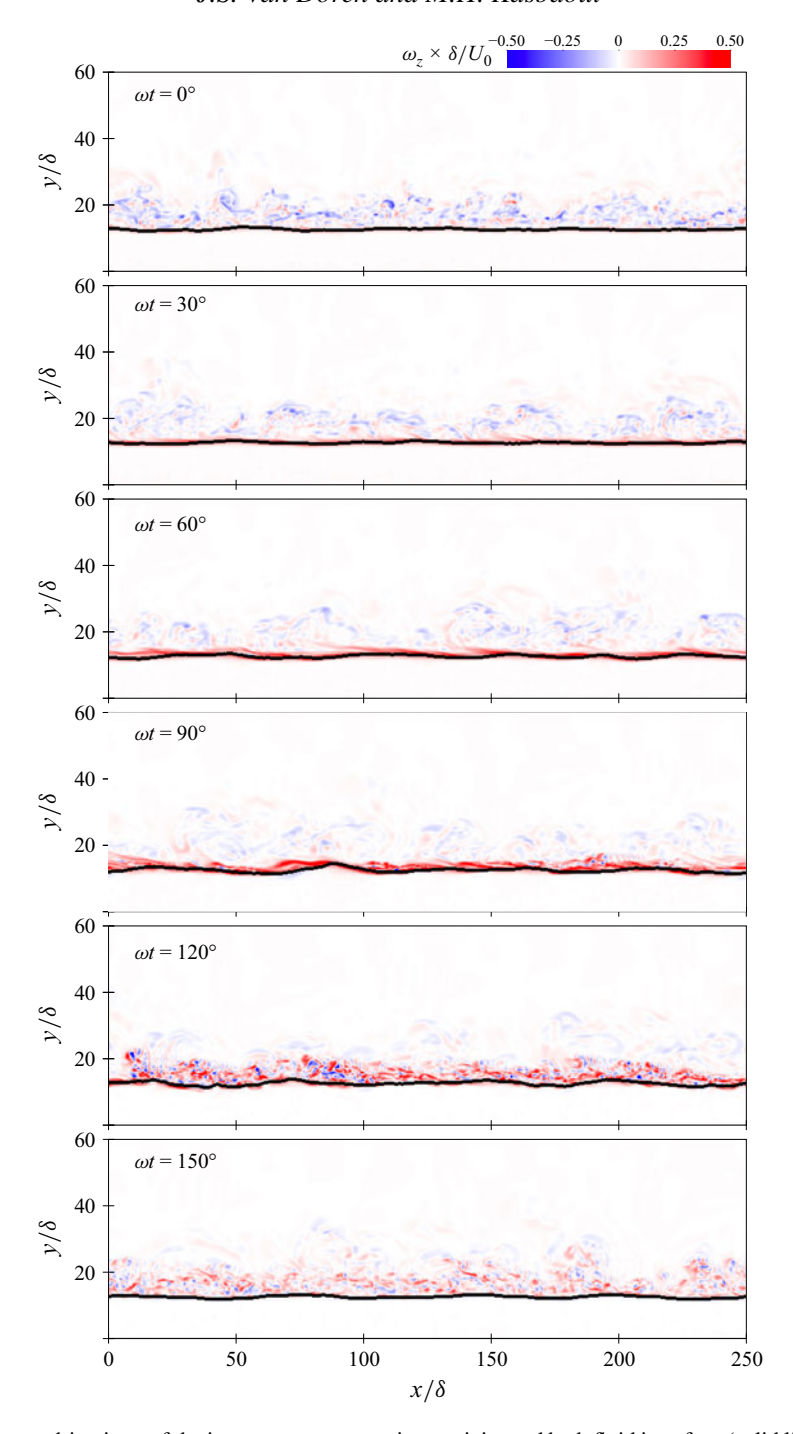


Figure 4. Zoomed-in views of the instantaneous spanwise vorticity and bed-fluid interface (solid line) at $Re_{\delta} = 400$. Increasing Reynolds number leads to greater flow disturbances and a dynamically evolving bed-fluid interface.

At $Re_{\delta} = 800$, figure 5 shows significant increase in flow disturbances over the bed, bed-fluid interface corrugations, and flow intrusion within the bed. The fluctuations' intensity and spatial extent largely exceed those due to intermittent turbulence in the case of an OBL over a smooth and impermeable wall. The flow intrusion within the particle bed is also much greater at $Re_{\delta} = 800$ compared to $Re_{\delta} = 400$. This likely contributes to the increased corrugation of the bed-fluid interface at this Reynolds number. Further, the bed-fluid interface is most corrugated around phases 60° , 90° and 120° , which correspond to the phases with largest flow intrusion.

4.2. Fluid statistics

Having established the qualitative dynamics of these flows in § 4.1, we now characterise the fluid phase with quantitative measures.

Figures 6(a), 6(c) and 6(e) show vertical profiles of phase-averaged mean streamwise fluid velocity $\langle u_f \rangle_{xz}$ from the cases with particle bed at $Re_\delta = 200$, 400 and 800. To better appreciate the change caused by the particle bed, we also report data from the companion runs with a bottom smooth and impermeable wall discussed in Appendix A. In this figure, y_b denotes the average bed height. We determine the latter by computing the average y location of the isovolume $\alpha = \alpha_b = 0.2$, which represents the bed-fluid interface.

At $Re_{\delta} = 200$, the average streamwise fluid velocity from the cases with a particle bed and smooth impermeable wall are sensibly close and follow the laminar Stokes solution. The notable differences include a marginally thicker boundary layer, a significant slip velocity $u_{f,I}$ at the bed-fluid interface $y = y_b$, which reaches up to $u_{f,I} \simeq 0.1~U_0$ at phase 60°, and interstitial flow that decays quickly within 1.5 δ of depth. These features are characteristic of permeable interfaces (Voermans *et al.* 2017), although their net effect on the average streamwise fluid velocity profiles at $Re_{\delta} = 200$ is limited.

With increasing Re_{δ} , the differences between cases with particle bed and cases with a smooth and impermeable wall accentuate as effects due to bed permeability effects increase. Most notably, we note the increase of the boundary layer thickness, interfacial slip velocity, and depth of the interstitial flow. At $Re_{\delta} = 400$, the interfacial slip velocity peaks at $u_{f,I} \simeq 0.17~U_0$ at phase 60° , while the flow extends below the bed–fluid interface by up to 9δ . At $Re_{\delta} = 800$, the maximum slip velocity increases to $u_{f,I} \simeq 0.52~U_0$, and the flow extends below the bed–fluid interface by up to $14~\delta$.

In addition to altering the mean velocity profiles, the presence of a particle bed leads to greater velocity fluctuations than in the smooth wall cases. Figures 6(b), 6(d) and 6(f) show the streamwise velocity fluctuations for each Reynolds number. While the root mean square (rms) of the streamwise velocity fluctuations $u_{f,rms}$ in cases with a smooth and impermeable wall at $Re_{\delta} = 200$ and 400 are identically zero, we note the existence of significant fluctuations in the cases with particle bed and at matching Reynolds numbers. For $Re_{\delta} = 200$, $u_{f,rms}$ peaks at approximately 13% of the velocity amplitude and approximately 1.4 δ above the bed. At $Re_{\delta} = 400$, $u_{f,rms}$ peaks at 13% of the velocity amplitude U_0 at phase 90° and approximately 1.5 δ above the bed. At $Re_{\delta} = 800$, the $u_{f,rms}$ profiles are widest, indicating that the flow disturbances extend to approximately 20δ – 30δ above the bed. The highest fluctuations occur at phase 90° and reach approximately 6.9% of the velocity amplitude. It is important to note that at $Re_{\delta} = 400$ and 800, velocity fluctuations are no longer homogeneous in the streamwise direction due to the waviness of the bed–fluid interface. For $Re_{\delta} = 400$ and 800, the velocity fluctuations drop to below 0.1% of the velocity amplitude (U_0) at 60δ from the bed–fluid interface.

The particle bed leads to a different condition at the bed-fluid interface as compared to a smooth wall. In the smooth wall case, no-slip applies at the wall, while the particle

J.S. Van Doren and M.H. Kasbaoui

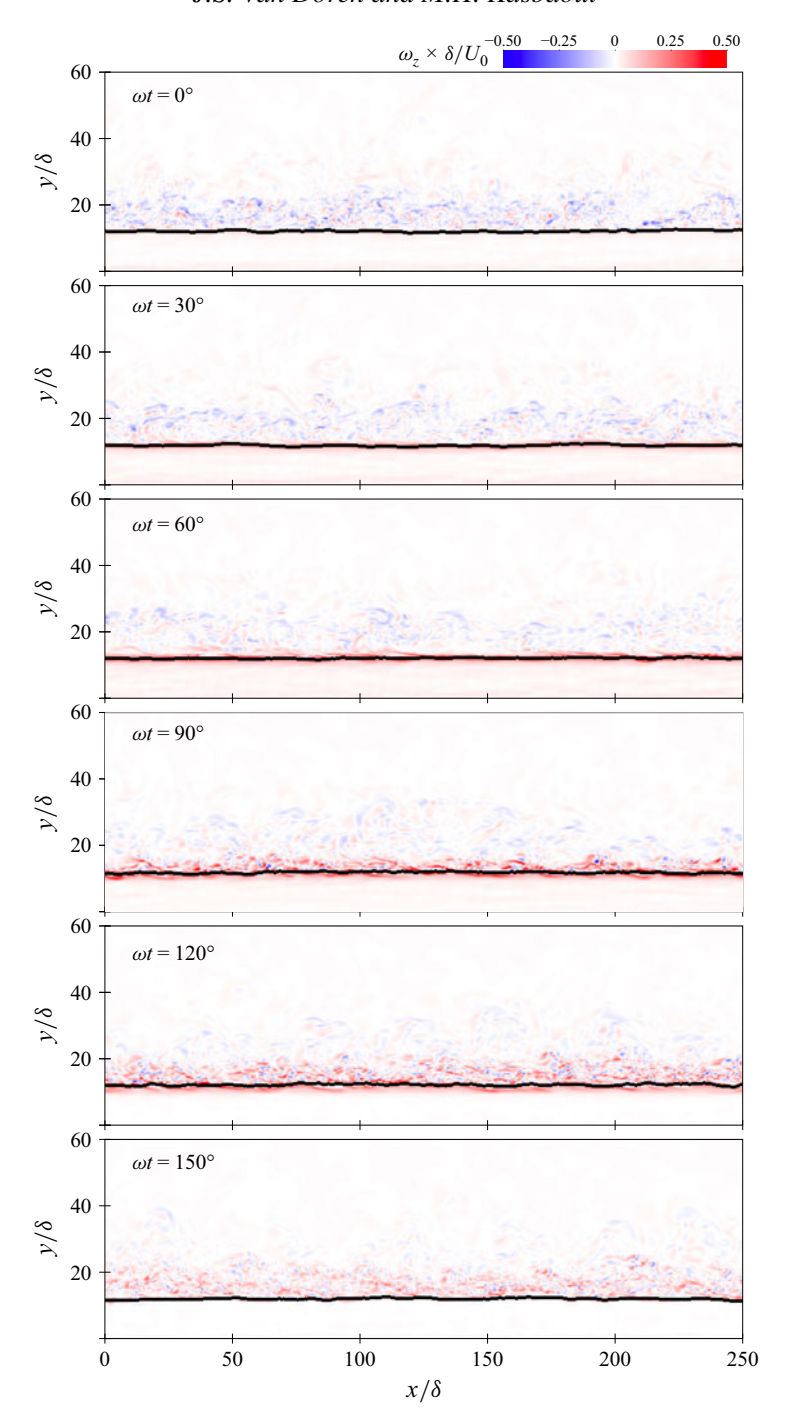


Figure 5. Zoomed-in views of the instantaneous spanwise vorticity and bed-fluid interface (solid line) at $Re_{\delta} = 800$. The bedform shifts into ripples at various phases. The shedding vortices create a large range of scales. The eddies penetrate the bed interface.

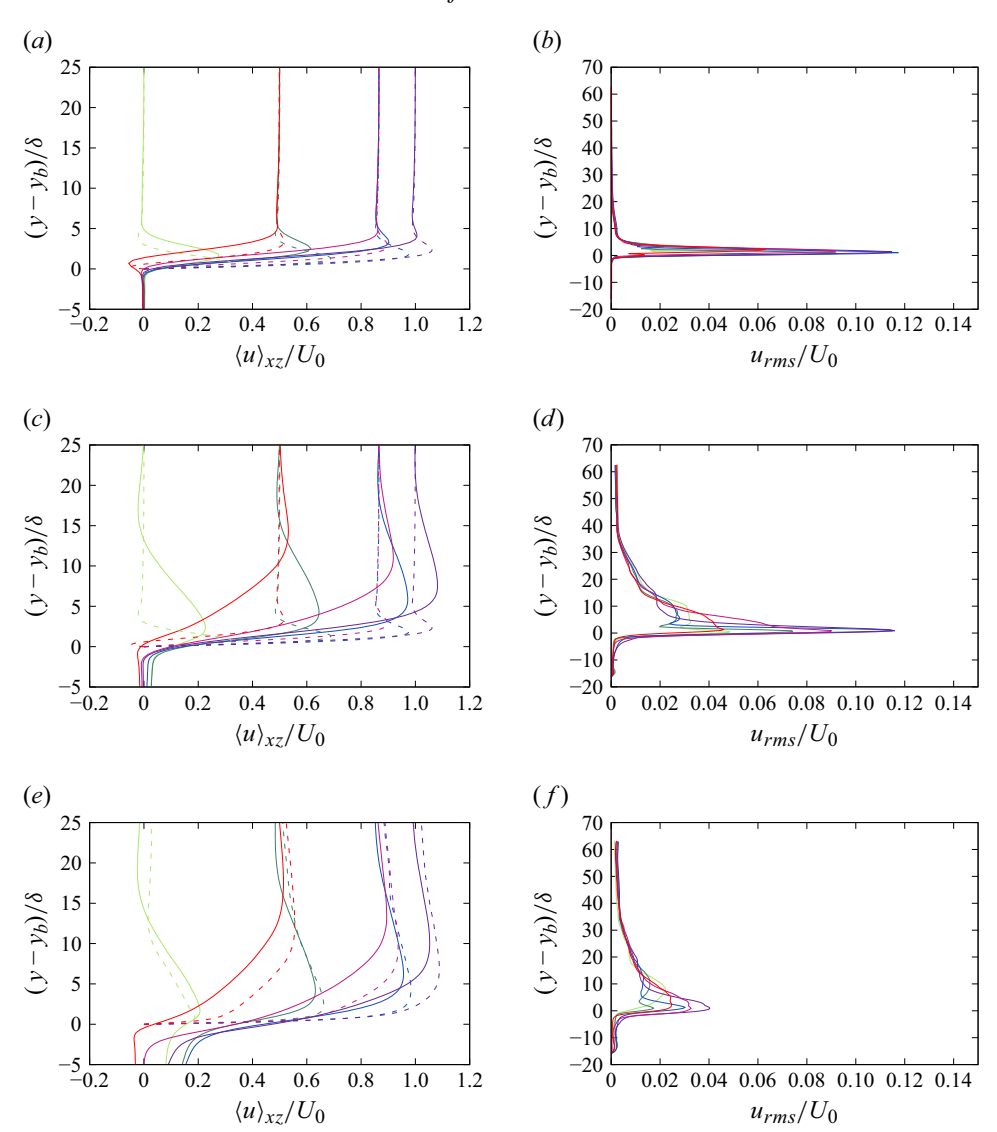


Figure 6. Statistics of the phase-averaged mean streamwise velocity at (a,b) $Re_{\delta} = 200$, (c,d) $Re_{\delta} = 400$, and (e,f) $Re_{\delta} = 800$. The lines correspond to phases $\omega t = 0^{\circ}$ (—), $\omega t = 30^{\circ}$ (—), $\omega t = 60^{\circ}$ (—), $\omega t = 90^{\circ}$ (—), $\omega t = 120^{\circ}$ (—), and $\omega t = 150^{\circ}$ (—). The dashed lines correspond to the smooth wall simulations from Appendix A.

bed is porous, which leads to a slip velocity at the bed-fluid interface. This causes the bed shear stress to drop compared to the smooth wall case. Predicting the sediment transport is dependent upon accurate values of the bed shear stress, or non-dimensionally, the Shields number θ . The Shields number can be estimated *a priori* using the single-phase wall shear stress, i.e. $\tau_w = \mu \left(\frac{\partial u}{\partial y} \right)|_{y=0}$. We denote this Shields number as $\theta_{wall} = \tau_w/((\rho_p - \rho_f)gd_p)$. Alternatively, the bed shear stress can be defined using the shear stress conditioned on an isosurface corresponding to the bed-fluid interface $\alpha_p = \alpha_{p,b}$ (Arolla & Desjardins 2015). We evaluate this in two ways. The first way follows the calculation of

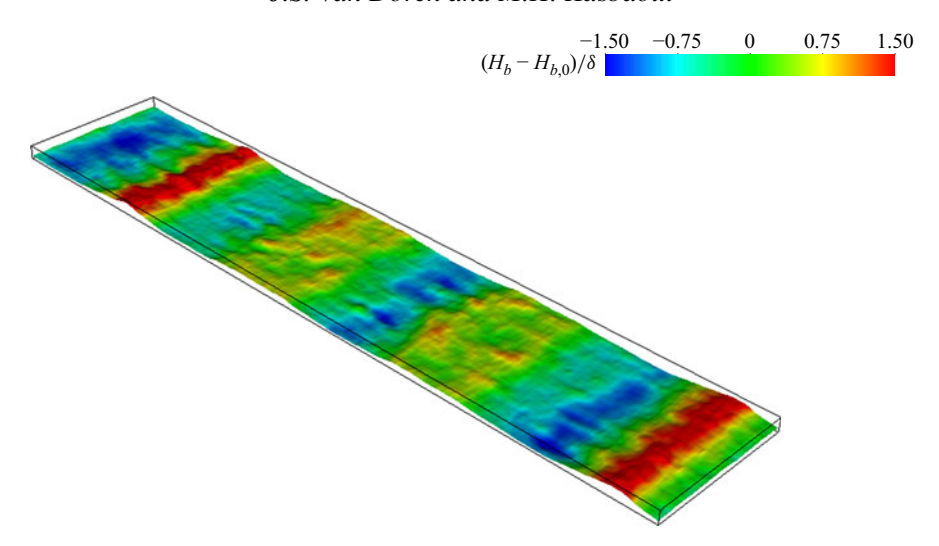


Figure 7. The $Re_{\delta} = 400$ bedform height deviations. Small ripples rise and fall below the average bed height.

Arolla & Desjardins (2015), i.e.

$$\tau_b = (\mu + \mu^*) \left\langle \frac{\overline{\partial u}}{\partial y} \right\rangle \bigg|_{y_b} = \mu \alpha^{-2.8} \left\langle \frac{\overline{\partial u}}{\partial y} \right\rangle \bigg|_{y_b}. \tag{4.1}$$

We denote the Shields number based on the expression above as $\theta_{bed}^{(1)}$. Note that this evaluation does not account for the waviness of the bedform. To deal with this, we carry out an alternative computation of the bed shear stress by interpolating the deviatoric stress tensor to the bed-fluid interface. Figure 7 shows an example of instantaneous isosurface $\alpha = \alpha_h$ representing the bed-fluid interface. In this second approach, we determine the bed shear τ_b using

$$\tau_b = \left\| \frac{1}{A_I} \iint_{S_I} \mathbf{n} \cdot \mathbf{\tau'} \, \mathrm{d}S \right\| \,, \tag{4.2}$$

where S_I represents the bed-fluid interface, A_I is the total interfacial area, \boldsymbol{n} is the normal vector on the isosurface $\alpha_p = \alpha_{p,b}$, and $\boldsymbol{\tau}' = \mu[\nabla \boldsymbol{u} + \nabla \boldsymbol{u}^{\mathrm{T}} - (2/3)(\nabla \cdot \boldsymbol{u})\boldsymbol{I}] + \boldsymbol{R}_{\mu}$ is the deviatoric stress tensor. With the closure of Gibilaro *et al.* (2007), this tensor reads

$$\boldsymbol{\tau}' = \mu \alpha_f^{-2.8} \left(\nabla \boldsymbol{u} + \nabla \boldsymbol{u}^{\mathrm{T}} - (2/3) (\nabla \cdot \boldsymbol{u}) \boldsymbol{I} \right). \tag{4.3}$$

We denote the resulting Shields number as $\theta_{bed}^{(2)}$.

Figure 8 shows the evolution of θ_{wall} , $\theta_{bed}^{(1)}$ and $\theta_{bed}^{(2)}$ during a full cycle. We also report the maximum Shields number obtained with each method in table 3. We note close agreement between $\theta_{bed}^{(1)}$ and $\theta_{bed}^{(2)}$ at all Reynolds numbers. This indicates that the bed waviness does not have a significant effect on the bed shear stress in these cases. Regardless of the method used, the Shields number estimated using the bed shear stress $(\theta_{bed}^{(1)}$ and $\theta_{bed}^{(2)})$ is much lower than the Shields number based on single-phase wall shear stress θ_{wall} , even at $Re_{\delta} = 200$. This was also noted by Kidanemariam & Uhlmann (2014) in PR-DNS of laminar channel flow with a sediment bed. They observed a progressive departure of the Shields number from the Poiseuille predictions with increasing fluid flow rate, caused by the departure of the flow profile from a strictly parabolic profile at the bed

Re_{δ}	θ_{wall}	$ heta_{bed}^{(1)}$	$\theta_{bed}^{(2)}$
200	0.0560	0.0296	0.0279
400	0.1121	0.0330	0.0423
800	0.2428	0.0504	0.0448

Table 3. Maximum values of the Shields number by method of computation.

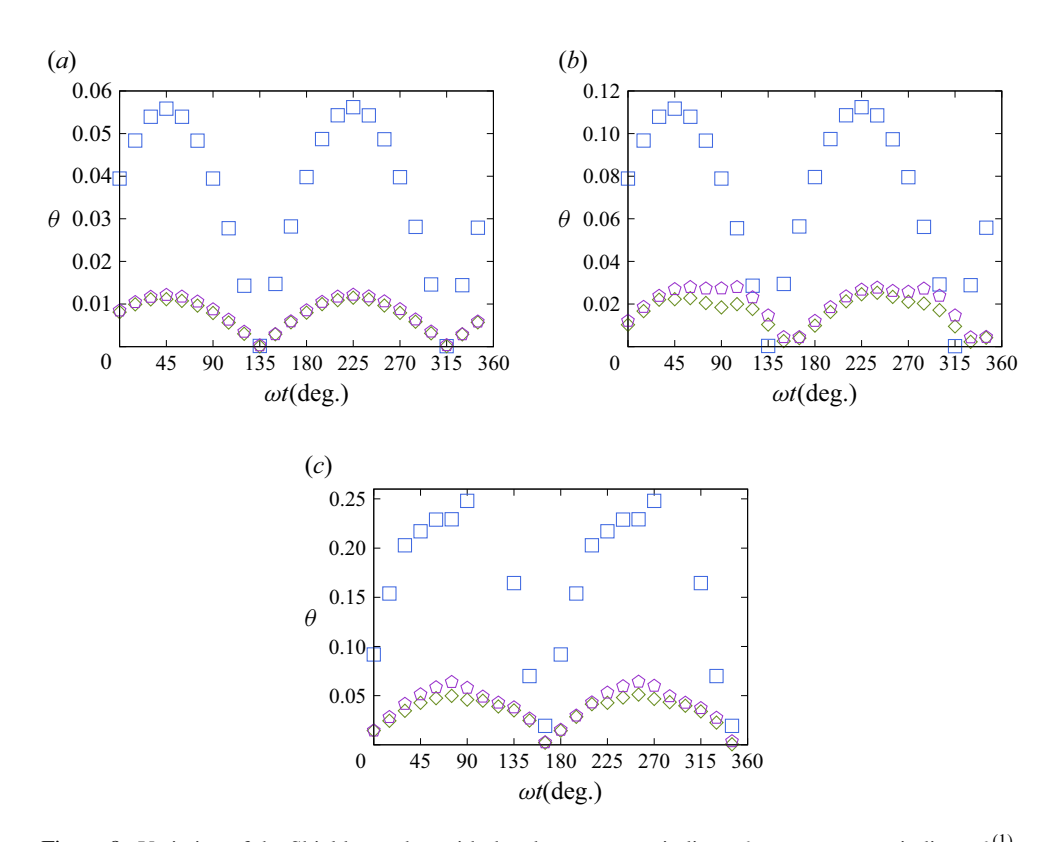


Figure 8. Variation of the Shields number with the phase: squares indicate θ_{wall} ; pentagons indicate $\theta_{bed}^{(1)}$; diamonds indicate $\theta_{bed}^{(2)}$. (a) $Re_{\delta} = 200$, (b) $Re_{\delta} = 400$ and (c) $Re_{\delta} = 800$.

interface. Likewise, flow intrusion through the sediment bed leads to lower gradients at the bed as shown in figure 6, which in turn leads to lower bed shear stress.

4.3. Particle statistics

Next, we analyse the characteristics of the particulate phase and how these relate to those of the fluid phase.

At $Re_{\delta} = 400$, the particle bed is characterised by the periodic particle transport at the ripple crests. This can be seen in figure 9(a), which depicts a top-down view of the particle bed between $\omega t = 0^{\circ}$ and $\omega t = 150^{\circ}$, and where the particles are coloured by their normalised streamwise velocities. At phase 0° , most particles are immobile and within the bed. From there, the rising fluid velocity initiates particle saltation at the ripple crests, which are well visible at phase 60° . These ripples are quasi-two-dimensional and display wavelength approximately $\sim 60\delta$. The rolling ripples continue intensifying until phase

J.S. Van Doren and M.H. Kasbaoui

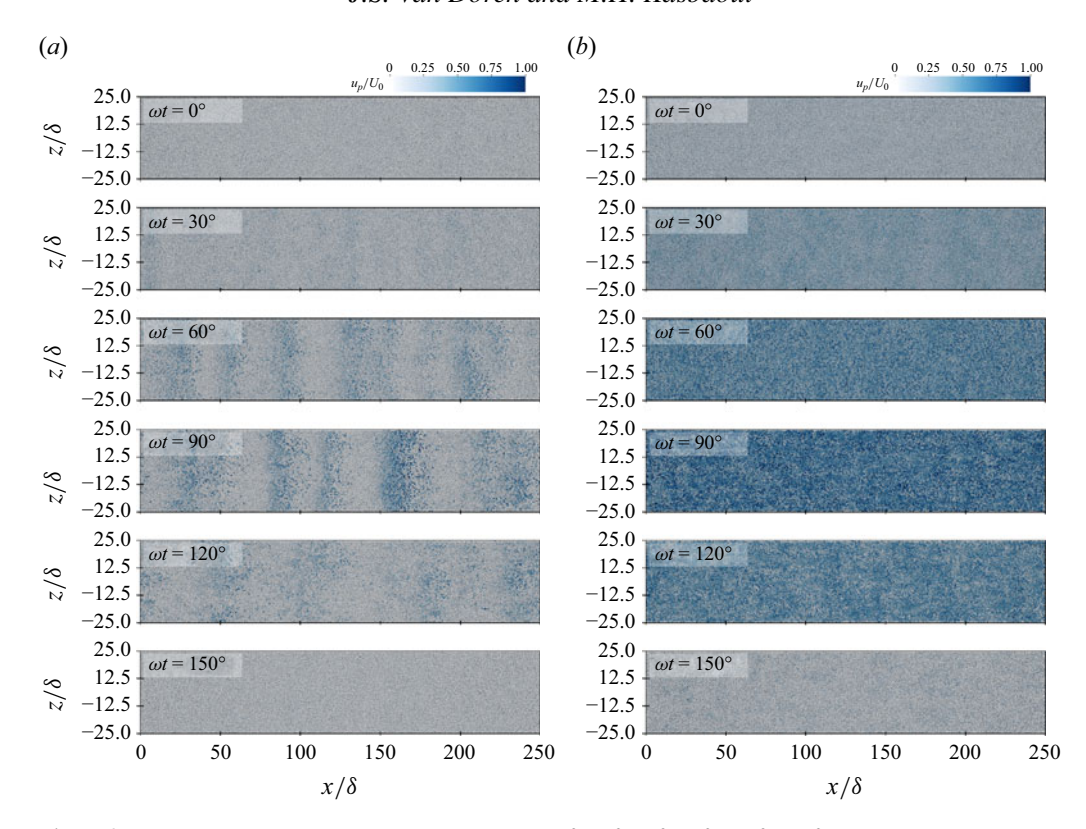


Figure 9. Top-down views of the particle bed at phases 0° , 30° , 60° , 90° , 120° , 150° for (a) $Re_{\delta} = 400$ and (b) $Re_{\delta} = 800$. The particles are coloured by their normalised streamwise velocity. The case at $Re_{\delta} = 400$ shows periodic rolling ripples, whereas the case at $Re_{\delta} = 800$ exhibits a particle suspension layer, and may be evolving towards a new bedform.

90°. After that, the decrease in fluid velocity leads to a slow down of the particles until all are immobile again by phase 150°. This process occurs again, albeit in the reverse direction, between phases 180° and 360°.

With increasing Re_{δ} to 800, the bed may be evolving towards a new bedform with wavelength greater than L_x . As shown in figure 9(b), the rolling ripples noted at $Re_{\delta} = 400$ are no longer present at $Re_{\delta} = 800$. Instead, we note the periodic emergence and collapse of a layer of suspended particles over the bed. At phase 0° , most particles start at rest in the bed. As the flow accelerates, particles in the top layer of the bed start saltating, which can be seen at phase 30° . As the fluid velocity continues increasing, more particles are set in motion. At phase 60° , we note that a large number of particles are suspended within the fluid column. The layer of suspended particles continues growing up to phase 120° , by which point the fluid velocity has begun decreasing. With the continued slowing down of the flow, most particles redeposit in the bed by phase 150° , while only few remain suspended.

Note that we do not present figures similar to figures 9(a) and 9(b) for the case at $Re_{\delta} = 200$ because particle motion is negligible in that case.

Figure 10 shows the bed surface interface averaged over the spanwise direction, for $Re_{\delta} = 400$ and 800. The different lines correspond to the interface locations from periods 2–10. At $Re_{\delta} = 400$, the bed–fluid interface in figure 10(a) develops into a clear bedform as the simulation progress. The wavelength associated with the ripples is $\lambda/\delta = 62.6$. The typical height of the ripples, measured from depression to peak, is approximately 4δ at

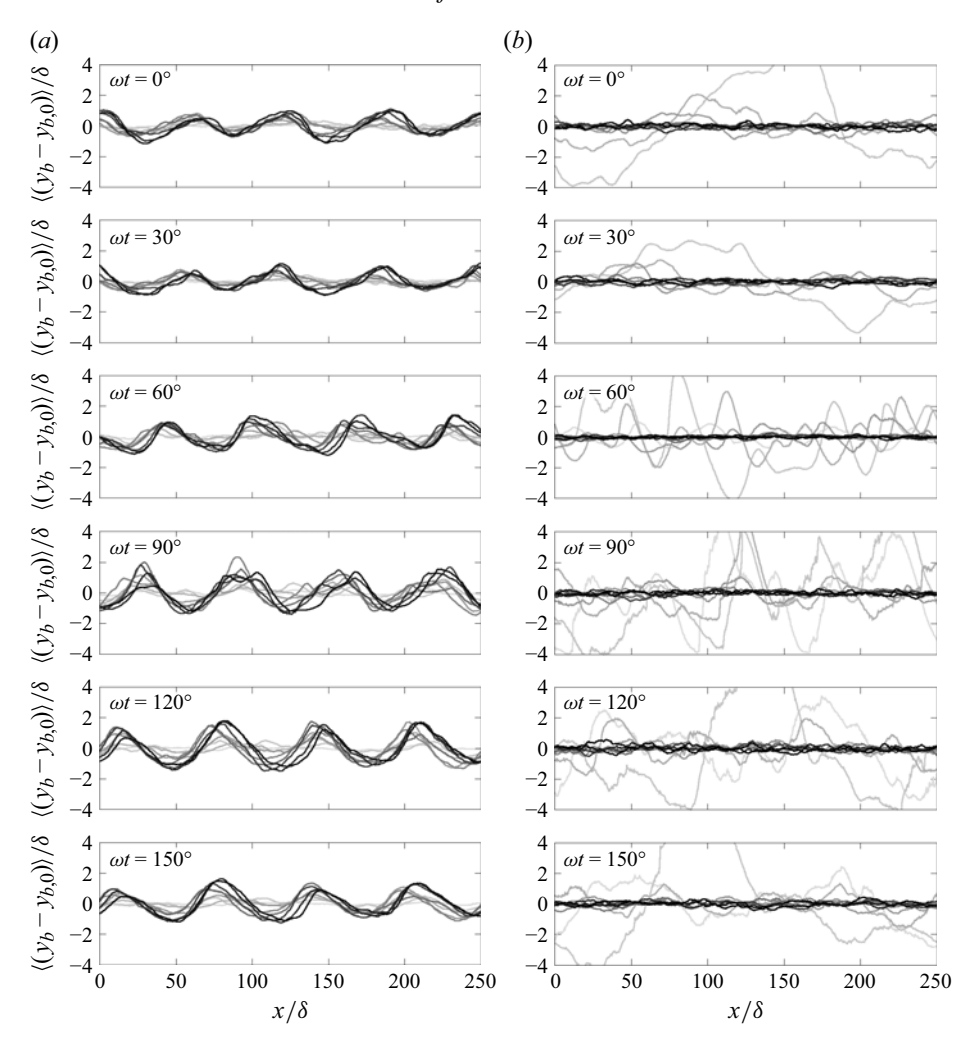


Figure 10. Bed interfaces for (a) $Re_{\delta} = 400$ and (b) $Re_{\delta} = 800$. Darker lines indicate later periods. For $Re_{\delta} = 400$, rolling-grain ripples emerge and move through the domain, but the dominant wavelength does not change. At $Re_{\delta} = 800$, the bed height becomes highly corrugated, and the bed-fluid interface breaks down.

phase 90°. While sediment particles move along the bed at significant velocities, as seen from figure 9(a), the bedform evolves on a much slower periodic time scale. At Re_{δ} = 800, the bed surface displays a range of small-scale corrugations. However, the large-scale ripples disappear. Figure 10(b) shows that the bed height deviations drop below 2δ . This is because particle transport takes place primarily in a suspension layer.

Next, we report the vertical profiles of normalised particle velocity in figures 11(a) and 11(b). At $Re_{\delta} = 400$, the normalised particle velocity is small, as $\langle \alpha_p u_p \rangle_{xz} / U_0 < 0.025$ for all phases. This indicates that the rolling ripples move at a velocity much smaller than the fluid velocity amplitude U_0 . The largest particle velocity occurs at phase 30° , in agreement with the qualitative observations from figure 9(a). We note that the particle velocity is non-zero only in a region of width $\sim 8\delta$ around the average bed height y_b . The width of this region is controlled by the height of the ripples, noted in figure 10(a), and is not due to suspended particles, as the latter are negligible at $Re_{\delta} = 400$. In contrast, the normalised particle velocity reaches significantly higher values and displays wider

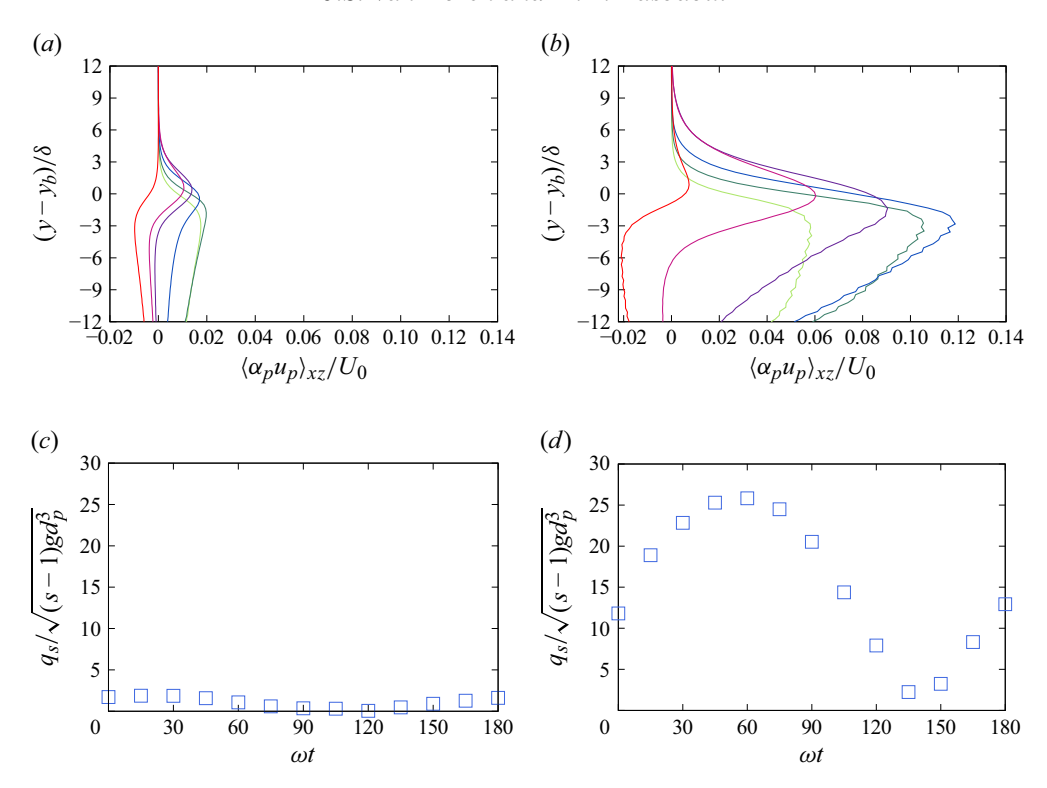


Figure 11. Normalised particle momentum profiles and mass fluxes at (a,c) $Re_{\delta} = 400$ and (b,d) $Re_{\delta} = 800$. The lines in (a,b) correspond to phases $\omega t = 0^{\circ}$ (—), $\omega t = 30^{\circ}$ (—), $\omega t = 60^{\circ}$ (—), $\omega t = 90^{\circ}$ (—), $\omega t = 120^{\circ}$ (—), and $\omega t = 150^{\circ}$ (—). Significant particle momentum is seen near the bed interface, indicating particle motion at approximately the bed interface.

distribution at $Re_{\delta}=800$. At phase 150° , the region of non-zero particle momentum is approximately 18δ thick and peaks at approximately $0.08\rho_{p}U_{0}$. The widening of the profile and the absence of large-scale deformations of the bed-fluid interface indicate that the amount of suspended particles is significantly larger at $Re_{\delta}=800$ compared to $Re_{\delta}=400$. This is also in agreement with the qualitative observations from figure 9(b).

With regards to the computational aspects, we note that the particle velocity is negligible at approximately $\sim 10\delta$ below the bed-fluid interface y_b at all phases and Re_δ considered. This shows that the particle bed in our simulations, which has initial height $H_b = 16.7\delta$, is sufficiently tall to capture the dynamics near the bed-fluid interface without interference from boundary conditions at the bottom of the domain.

Figures 11(c) and 11(d) show the evolution of the normalised sediment flow rate q_s over a half-period, for $Re_{\delta} = 400$ and 800. We compute q_s by integrating the particle velocity profiles over the vertical direction, i.e.

$$q_s = \int_0^{L_y} \langle \alpha_p u_p \rangle_{xz} \, \mathrm{d}y. \tag{4.4}$$

At $Re_{\delta}=400$, the sediment volumetric flux peaks at 1.76 at phase $\omega t=30^{\circ}$. Notably, the sediment transport is not symmetric for the accelerating and decelerating portions of the periods. At $Re_{\delta}=800$, the sediment flux is more than 12 times greater than at $Re_{\delta}=400$. The maximum normalised flux is 25.8 at phase 60° . Here, too, we note an asymmetry between the acceleration and deceleration portions of the period.

5. Discussion and conclusions

In this study, we analyse data obtained from Euler-Lagrange simulations of an oscillatory boundary layer (OBL) developing over a bed of collisional and freely moving sediment grains with density ratio $\rho_p/\rho_f=2.65$ and Galileo number Ga=51.9. In these simulations, we vary the velocity amplitude to yield Reynolds numbers $Re_\delta=200-800$. The maximum Shields number based on the smooth wall case also varies from 5.60×10^{-2} to 2.43×10^{-1} , and the Keulegan-Carpenter number varies from 134.5 to 538.0. Companion simulations of an OBL over a smooth and impermeable wall show that the boundary layer follows the laminar Stokes solution at $Re_\delta=200$ and $Re_\delta=400$, and displays intermittent turbulence at $Re_\delta=800$. However, the presence of a mobile bed alters the flow characteristics and leads to a coupling of the dynamics of the OBL with that of the sediment bed.

The coupled dynamics arise from two fundamental mechanisms. The first one relates to the bed permeability. This is due to the porosity of the bed, which allows the flow to penetrate within the sediment layers. The extent of the flow penetration depends on the Reynolds number. In the case $Re_{\delta} = 200$, the flow penetration is of the order of the Stokes thickness δ . With increasing Re_{δ} , the flow penetration increases to approximately 9δ and 14δ at $Re_{\delta} = 400$ and $Re_{\delta} = 800$, respectively. Another consequence of the bed permeability is the emergence of a slip velocity at the bed–fluid interface. At phase 30° of the cycle, the interfacial slip velocity peaks at approximately $0.12U_0$ at $Re_{\delta} = 200$, $0.17U_0$ at phase 60° for $Re_{\delta} = 400$, and $0.52U_0$ at phase 90° for $Re_{\delta} = 800$. This significant slip leads to a thickening of the boundary layer and reduction of the bed shear stress.

The second fundamental mechanism that couples the dynamics of the particle bed and the OBL relates to particle motion. In the case $Re_{\delta} = 200$, the particles remain immobile during the entire cycle. This is expected because the maximum Shields number based on the shear stress at the bed-fluid interface in this case $(\theta_{max} = 1.21 \times 10^{-2})$ is below the critical Shields number for incipient motion. Thus the only changes to the OBL in this case are those due to permeability. At $Re_{\delta} = 400$ and 800, the particles become mobile and lead to a dynamic evolution of the sediment bed. At $Re_{\delta} = 400$, the particles form rolling-grain ripples. The latter emerge from small-scale corrugations in the bed-fluid interface. These corrugations coarsen very quickly and lead to a bedform with height 4δ and wavelength approximately $\sim 60\delta$. Analysing the vorticity dynamics shows that these ripples cause enhanced vortex shedding in the flow, which leads to fluid velocity disturbances similar to those observed in the disturbed laminar regime. At $Re_{\delta} = 800$, the intermittent turbulence leads to the formation of a particle transport layer. Between phases 60° and 120° of the half-cycle, the bed-fluid interface recedes slightly and a layer of suspended particles forms. During the rest of the half-cycle, the suspended particles settle into the bed and become nearly motionless at phase 0°. Because of their large momentum and their feedback force on the fluid, the suspended particles induce significant fluctuations in the flow. This leads to further widening of the boundary layer and greater fluctuations than is observed in the corresponding particle-free case.

In this work, we have also shown that the dynamics of sediment beds under a wide range of oscillatory and unsteady flow conditions can be predicted at reasonable computational cost using carefully designed Euler–Lagrange simulations. While PR-DNS require few to no models, their large computational cost often makes them too restrictive. In comparison with the PR-DNS of Mazzuoli *et al.* (2020), our simulations have domains 100 times larger: approximately 10 times longer in the streamwise direction, approximately 4 times wider in the spanwise direction, and about twice as tall. This allows us to capture bedforms, which was not possible in Mazzuoli *et al.* (2020). Further, we were able to simulate 10

cycles for each of our cases, compared to 1–4 cycles in Mazzuoli *et al.* (2020). The computational cost of these simulations is approximately 400 000 CPU-hours per case (equivalent to about 15 days of run time on 1152 CPUs), which is attainable for many researchers with today's computational resources.

Acknowledgements. Computing resources through ACCESS award EES230041 and Research Computing at Arizona State University are gratefully acknowledged.

Funding. This research received no specific grant from any funding agency, commercial or not-for-profit sectors.

Declaration of interests. The authors report no conflict of interest.

Appendix A. Structure of an OBL over a smooth wall

In this appendix, we present a detailed description of the flow characteristics at $Re_{\delta} = 200$, 400 and 800, where the bottom boundary is an impermeable smooth wall rather than a sediment bed. The reasons for this are twofold. First, analytical solutions exist for the laminar regime, which allows the validation of the computational approach. Second, these runs serve as a benchmark to elucidate the changes to the flow in the presence of a sediment bed.

Figure 12 shows the normalised spanwise vorticity field at phases $\omega t = 0$, 30, 60, 90, 120, and 150 degree for the case $Re_{\delta} = 400$. The solution for $Re_{\delta} = 200$ shows vorticity structure similar to that of the $Re_{\delta} = 400$ solution, thus is not included here. The vorticity in these low Reynolds number cases is organised into sheets in the near-wall region. This indicates laminar flow, so the flow at $Re_{\delta} = 200$, 400 should obey the Stokes solution

$$u_{f,x}/U_0 = \cos(\omega t) - e^{-y/\delta}\cos(\omega t - y/\delta), \tag{A1}$$

$$u_{f,y}/U_0 = 0.$$
 (A2)

To verify this, we compare the Stokes solution to vertical profiles of the phase-averaged fluid velocity from the simulation at $Re_{\delta} = 400$ in figure 13. The agreement between the simulated data and the analytical solution is excellent, showing that the flow is indeed laminar at these Reynolds numbers. This also validates the computational approach for an impermeable smooth wall OBL at low Reynolds numbers.

As an additional comparison, we compute the coefficient of friction C_f defined as

$$C_f = \frac{|\tau_w|}{(1/2)\rho_f U_0^2},\tag{A3}$$

where τ_w is the wall shear stress. Figure 14 shows the variation of the coefficient of friction scaled by Re_δ to cancel the Reynolds number dependence of the coefficient of friction. The scaled coefficient is plotted over a period for the cases of an OBL over an impermeable smooth wall at $Re_\delta = 200$ and 400, alongside the Stokes solution. Here, too, the agreement between numerical and Stokes solution is excellent, which further demonstrates that the OBL at these Reynolds numbers is fully laminar.

Unlike the lower Reynolds number cases, figure 15 shows significant vorticity throughout the cycle for the case at $Re_{\delta} = 800$. Of particular interest is the range of scales seen at phase 120°, which is in the decelerating portion of the cycle. This eruption of velocity fluctuations, followed by partial relaminarisation, is characteristic of the intermittent turbulence regime. Similar observations were made by Jensen *et al.* (1989), Vittori & Verzicco (1998) and Salon *et al.* (2007).

While the vorticity field for $Re_{\delta} = 800$ shows a range of eddies, strict wall-bounded turbulence requires the existence of a logarithmic layer. To this end, we report in figure 16

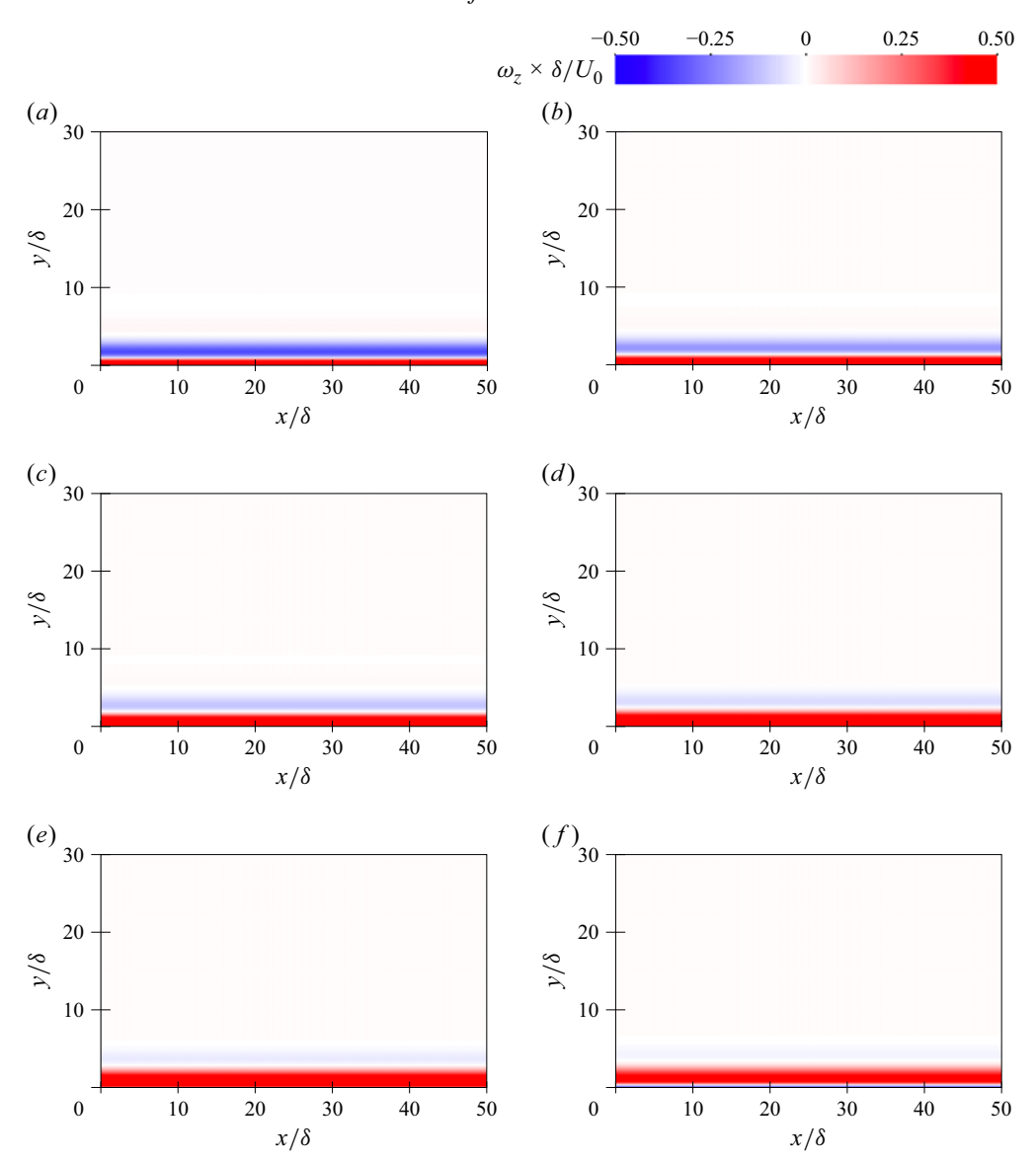


Figure 12. Normalised spanwise vorticity fields at $Re_{\delta} = 400$ for a smooth, impermeable wall, at phases 0°, 30°, 60°, 90°, 120°, 150°. The vorticity is arranged in laminae at all phases. (a) $\omega t = 0^{\circ}$, (b) $\omega t = 30^{\circ}$, (c) $\omega t = 60^{\circ}$, (d) $\omega t = 90^{\circ}$, (e) $\omega t = 120^{\circ}$ and (f) $\omega t = 150^{\circ}$.

vertical profiles of the spatially averaged streamwise velocity normalised using wall units, i.e. the friction velocity $u_{\tau} = \sqrt{\tau_w/\rho_f}$ as velocity scale, and v/u_{τ} as length scale. Since none of the phases shows a strict logarithmic layer, we conclude that the flow at $Re_{\delta} = 800$ is not fully turbulent, despite presenting significant fluctuations.

In Euler-Lagrange simulations, the choice of filter width δ_f is an important modelling consideration. To justify the point-particle approximation, δ_f must be much larger than the particle size d_p . Yet resolving the vortical structures requires δ_f to also be as small as possible. For the present study, we chose $\delta_f = 5d_p$. As recently shown in Hausmann *et al.*

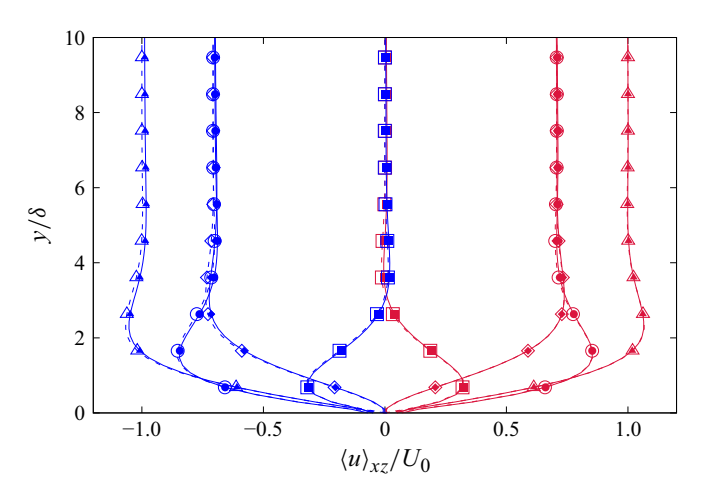


Figure 13. Normalised streamwise velocity for the case of an OBL over an impermeable smooth wall at $Re_{\delta} = 400$. Filled symbols correspond to the Stokes solution, while open symbols correspond to smooth wall simulations. To differentiate the positive and negative portions of the period, we plot the positive half-cycle in red, and the negative half-cycle in blue. The symbols indicate the phase: \Box for $\omega t = 0^{\circ}$, 180° , \odot for $\omega t = 45^{\circ}$, 225° , \triangle for $\omega t = 90^{\circ}$, 270° , \odot for $\omega t = 135^{\circ}$, 315° . The strong agreement between the simulated data and the Stokes solution indicates that the flow is fully laminar in this case.

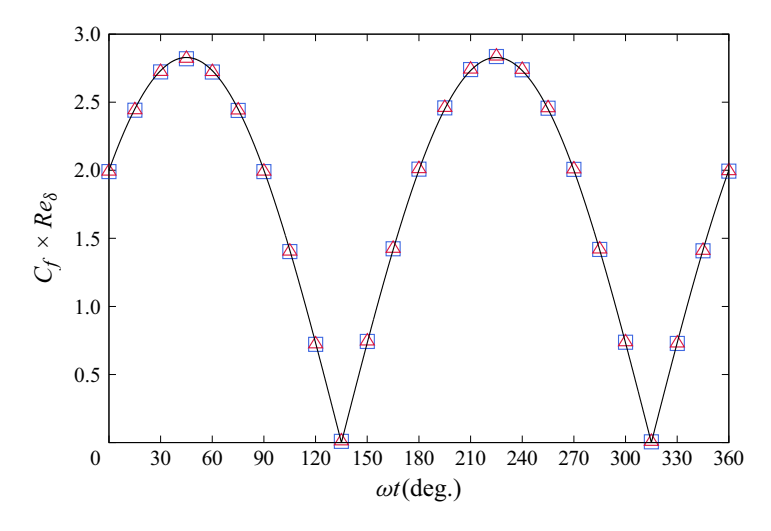


Figure 14. Scaled coefficient of friction over one period at $Re_{\delta} = 200$ and 400, for a smooth, impermeable wall. The black line correspond to the Stokes solution. Symbols correspond to the numerical solution: \Box for $Re_{\delta} = 200$, and \triangle for $Re_{\delta} = 400$. All cases collapse onto the Stokes solution.

(2024), this filter size reduces errors associated with the point-particle approximation, while providing adequate resolution.

To show the impact of filter size on the fluid statistics, we performed additional simulations of the case at $Re_{\delta} = 800$ with filter sizes $\delta_f = 3d_p$, $5d_p$ and $7d_p$. Note that $\delta_f = 3d_p$ is generally considered to be too small to justify the point-particle approximation, while $\delta_f = 5d_p$ and $\delta_f = 7d_p$ are values commonly used in the literature (Capecelatro & Desjardins 2013*a*; Hausmann *et al.* 2024).

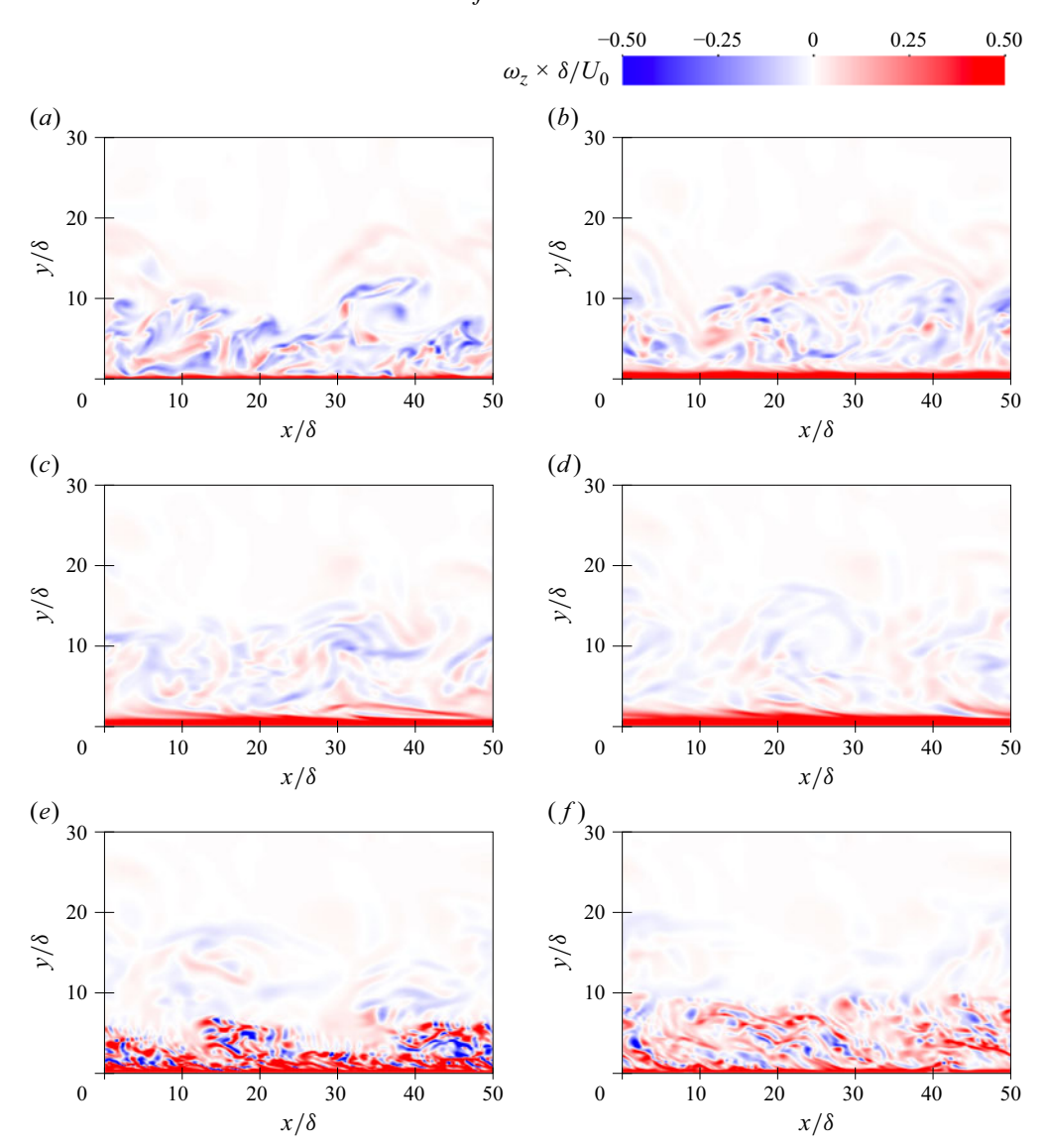


Figure 15. Normalised spanwise vorticity field in DNS of an OBL over an impermeable smooth wall at $Re_{\delta} = 800$, for a smooth, impermeable wall. The eruption of velocity fluctuations during the decelerating portion of the cycle (120° and 150°) indicates that this flow is in the intermittent turbulent regime. (a) $\omega t = 0^{\circ}$, (b) $\omega t = 30^{\circ}$, (c) $\omega t = 60^{\circ}$, (d) $\omega t = 90^{\circ}$, (e) $\omega t = 120^{\circ}$ and (f) $\omega t = 150^{\circ}$.

Figure 17 shows the impact of varying the filter size on mean and rms fluctuations of the streamwise velocity at phases 0° , 90° and 150° . We note that, as expected, $\delta_f = 3d_p$ shows the largest deviation. The results at $\delta_f = 5d_p$ and $\delta_f = 7d_p$ are sensibly similar, which justifies our choice of $\delta_f = 5d_p$ for the remaining simulations.

The reader interested in further details on the role of filter size in Euler–Langrange modelling is referred to Hausmann *et al.* (2024).

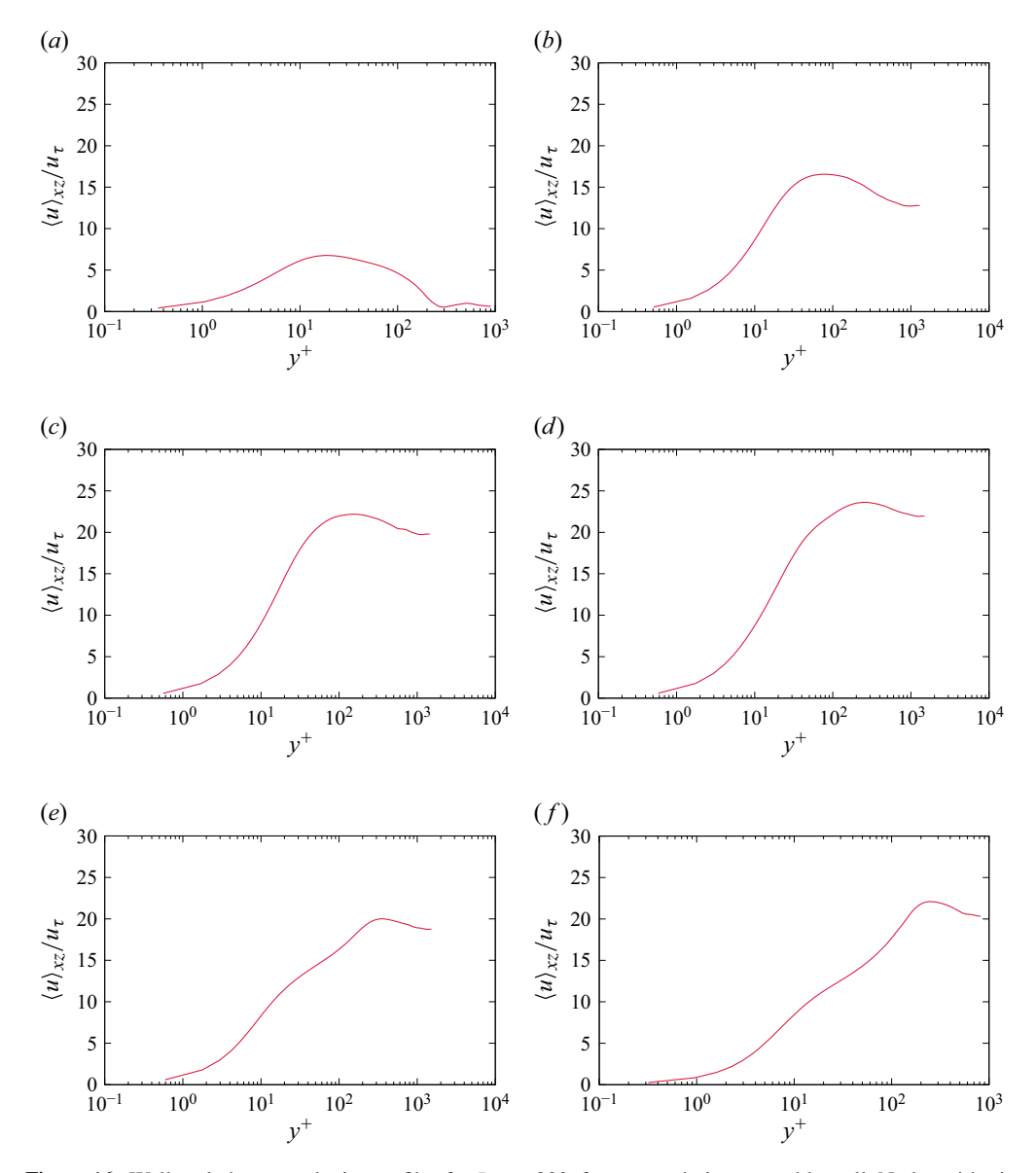


Figure 16. Wall scaled mean velocity profiles for $Re_{\delta} = 800$, for a smooth, impermeable wall. No logarithmic layer is observed. (a) $\omega t = 0^{\circ}$, (b) $\omega t = 30^{\circ}$, (c) $\omega t = 60^{\circ}$, (d) $\omega t = 90^{\circ}$, (e) $\omega t = 120^{\circ}$ and (f) $\omega t = 150^{\circ}$.

Appendix B. Review of the soft-sphere collision model

The soft-sphere collision model is dependent upon the parameters k and η , which are the spring stiffness and damping factor, respectively. They are related to the reduced mass $m_{ab} = (1/m_a + 1/m_b)^{-1}$, collision time τ_{col} , and coefficient of restitution e, as

$$k = \frac{m_{ab}}{\tau_{col}^2} (\pi^2 + \ln(e)^2), \tag{B1}$$

$$k = \frac{m_{ab}}{\tau_{col}^2} (\pi^2 + \ln(e)^2),$$

$$\eta = -2 \ln(e) \frac{\sqrt{m_{ab}k}}{\sqrt{\pi^2 + \ln(e)^2}}.$$
(B1)

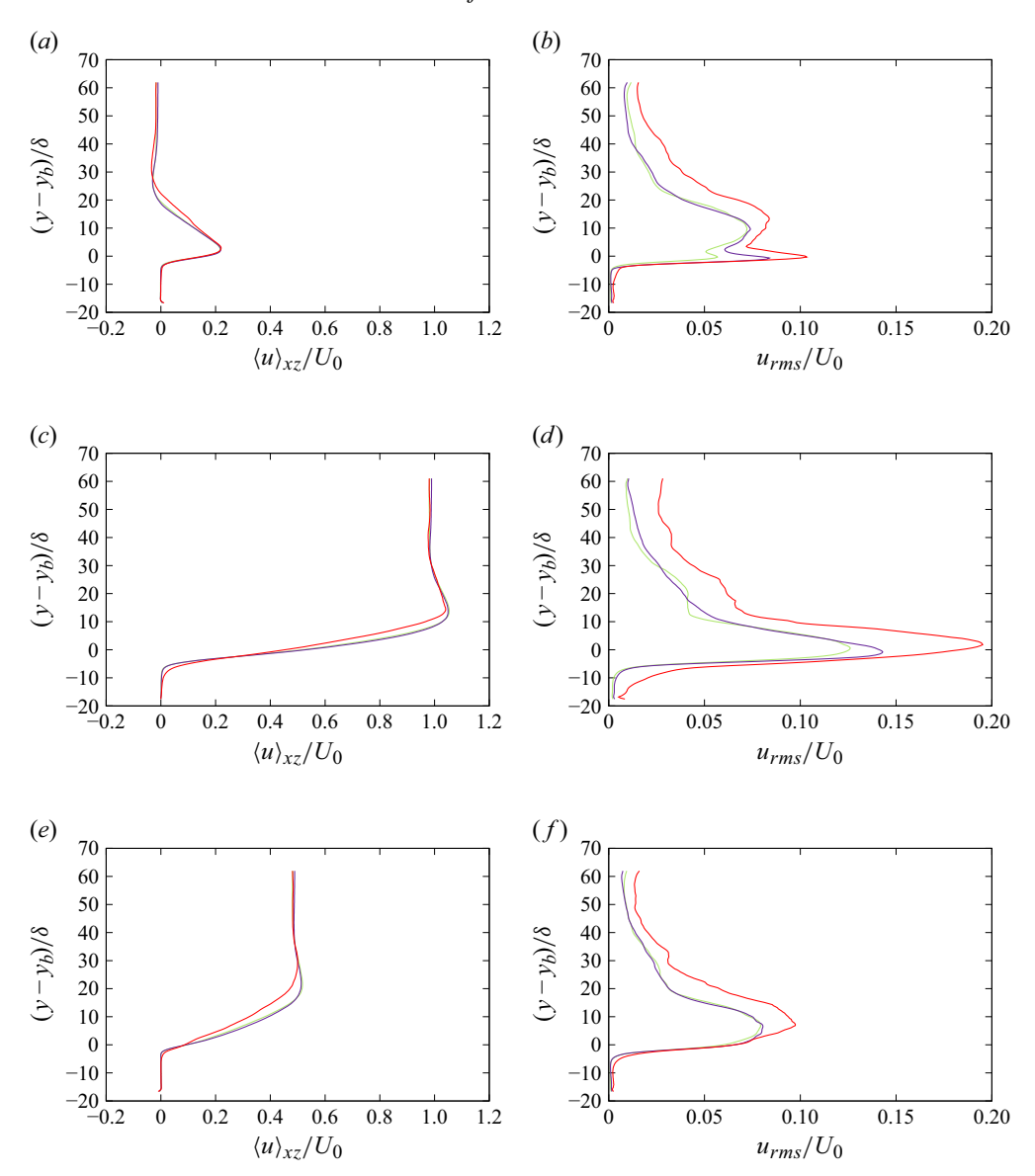


Figure 17. Statistics of the streamwise fluid velocity for filter widths $\delta_f = 3d_p$ (—), $5d_p$ (—) and $7d_p$ (—): (a,c,e) mean and (b,d,f) rms fluctuations. There is little difference between results with $\delta_f = 5d_p$ and $\delta_f = 7d_p$, which indicates that either value is a good choice in Euler–Lagrange simulations. (a) $\omega t = 0^\circ$, (b) $\omega t = 30^\circ$, (c) $\omega t = 60^\circ$, (d) $\omega t = 90^\circ$, (e) $\omega t = 120^\circ$ and (f) $\omega t = 150^\circ$.

The radius of influence λ allows us to robustly handle high-speed collisions by initiating the collision of high-speed particle pairs just before contact. Following Finn *et al.* (2016), λ is calculated as

$$\lambda = \frac{\lambda_0}{2} (d_{p,a} + d_{p,b}) \left(\frac{\text{CFL}_{ab}^c}{\text{CFL}_{max}^c} \right), \tag{B3}$$

where the collisional CFL number is $\text{CFL}_{ab}^c = (2 | \boldsymbol{u}_{ab,n} | \Delta t)/(d_p^a + d_p^b)$, and λ_0 is the maximum radius of influence permitted when the collision occurs at the maximum

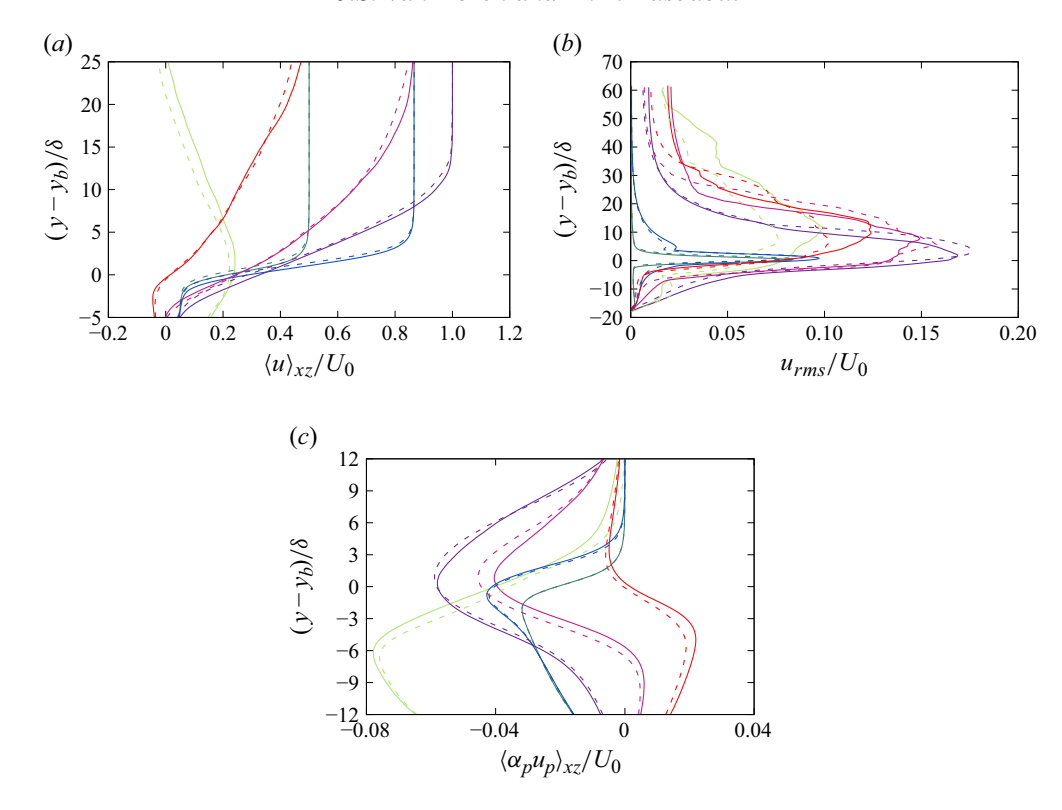


Figure 18. Profiles of mean fluid velocity and rms velocity fluctuations at $Re_{\delta} = 800$. Solid lines correspond to the grid described in the main text, while dashed lines correspond to the refined grid. Lines colours correspond to phases $\omega t = 0^{\circ}$ (—), $\omega t = 30^{\circ}$ (—), $\omega t = 60^{\circ}$ (—), $\omega t = 90^{\circ}$ (—), $\omega t = 120^{\circ}$ (—), and $\omega t = 150^{\circ}$ (—). The agreement is close, showing that the simulation is grid converged.

collision CFL number, CFL_{max}^c . The tangential collision force is modelled according to a static friction model

$$f_{p,t}^{c,b\to a} = -\mu_s |f_{p,t}^{c,b\to a}| t_{ab},$$
 (B4)

where t_{ab} is the tangential direction, and μ_s is the static friction coefficient. Collisions with walls are treated in the same way as above, but with the wall having infinite mass.

Appendix C. Grid convergence study

In order to demonstrate grid independence, we conduct a simulation at $Re_{\delta} = 800$ with grid resolution $N_x \times N_y \times N_z = 672 \times 422 \times 134$, and compare the results to the simulation with resolution $N_x \times N_y \times N_z = 672 \times 211 \times 134$, for one period. Thus the wall-normal resolution is twice that in the coarser grid. Note that we do not refine the grid in the streamwise and spanwise directions because the gradients are primarily in the wall-normal direction, and the resolution in the streamwise and spanwise directions already exceeds the requirements for an OBL over a smooth wall. That is, the resolutions in the smooth wall case described in Appendix A are 0.78δ and 0.39δ in the streamwise and spanwise directions, respectively, while the resolution is 0.37δ in all directions for the bed cases.

In figure 18, we compare the fluid streamwise velocity profile, streamwise velocity fluctuations, and streamwise particle velocity. Increasing the resolution does not lead to

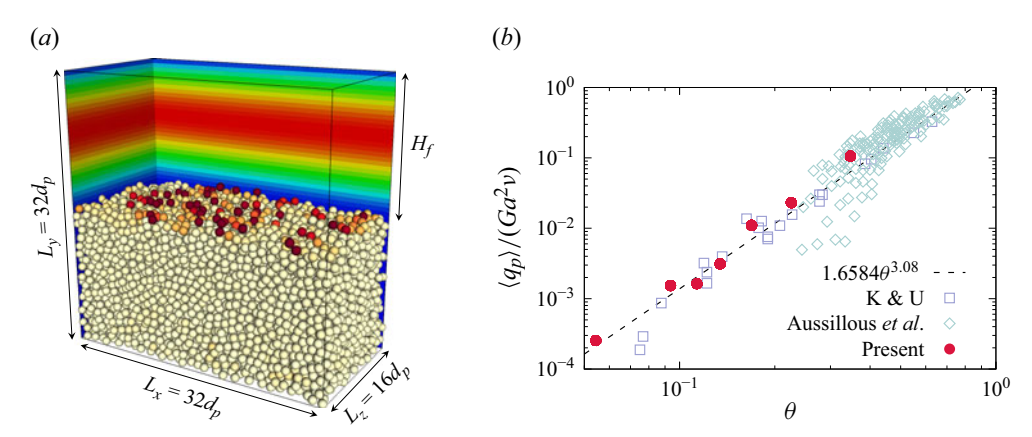


Figure 19. Sediment transport in a laminar channel flow: (a) schematic of the configuration in our simulations, and (b) variation of the normalised sediment flow rate with Shields number. The PR-DNS data are from Kidanemariam & Uhlmann (2014). The experimental data are from Aussillous et al. (2013). Despite not capturing flow features at the particle scale, our method captures the variation of sediment transport with Shields number very well.

significant change in these statistics. This indicates that our resolution choice in this study is adequate up to $Re_{\delta} = 800$.

Appendix D. Validation of the present Euler-Lagrange method for sediment transport

To demonstrate the capability of the present model to capture accurate sediment transport, we reproduce numerically the experiments of Aussillous *et al.* (2013) of bedload transport in a channel flow.

Following earlier numerical effort in Kidanemariam & Uhlmann (2014), Charru *et al.* (2016) and Rao & Capecelatro (2019), we set up our numerical analogue as shown in figure 19(a). The sediment grains are monodisperse with diameter d_p , restitution coefficient e=0.3, and friction coefficient $\mu_c=0.4$ (Kidanemariam & Uhlmann 2014). The domain dimensions are $32d_p$ in the streamwise direction, $32d_p$ in the vertical direction, and $16d_p$ in the spanwise direction. We use a uniform grid with spacing $\Delta x = d_p/2$, the same as in the main study.

The main non-dimensional numbers that control this problem are the bulk Reynolds number $Re = q_f/v$, where q_f is the fluid flow rate, Galileo number Ga, density ratio ρ_p/ρ_f , and Shields number θ . Following Kidanemariam & Uhlmann (2014), Charru *et al.* (2016) and Rao & Capecelatro (2019), and to enable comparisons with Aussillous *et al.* (2013), we define the Shields number based on the wall shear stress from a laminar Poiseuille flow. As discussed by Kidanemariam & Uhlmann (2014), this results in the following expression for the Shields number:

$$\theta = \frac{6Re}{Ga^2} \left(\frac{d_p}{H_f}\right)^2. \tag{D1}$$

Note that we determine the fluid column height H_f using the same approach outlined in Kidanemariam & Uhlmann (2014) and Rao & Capecelatro (2019).

Following Kidanemariam & Uhlmann (2014), we fix the bulk Reynolds number at Re = 375, density ratio at $\rho_p/\rho_f = 2.5$, and Galileo number at Ga = 8.56. We vary the Shields number from 0.05 to 0.35 by varying the bed height H_b . Similar to the main study, we

J.S. Van Doren and M.H. Kasbaoui

drive the flow using a pressure gradient forcing, which is constant here. The flow reaches a steady state after approximately $200H_b/U_b$, where U_b is the bulk velocity, at which point we start collecting data.

Despite not resolving flow features at the particle scale, the methodology and computational methods outlined in this paper are well capable of reproducing meso-scale dynamics, including bedload sediment transport. This is well evidenced in figure 19(b), which shows the variation of the normalised sediment $q_s/(Ga^2v)$ flux with Shields number. The figure shows our data alongside data from the experiments of Aussillous *et al.* (2013), PR-DNS of Kidanemariam & Uhlmann (2014), and their correlation $q_s/(Ga^2v) = 1.6584 \,\theta^{3.08}$. As is clearly shown in figure 19(b), the present methodology yields good agreement with experimental and PR-DNS data. The variation of the normalised sediment flow rate is well captured across three orders of magnitude. It follows a cubic law, similar to the one determined by Kidanemariam & Uhlmann (2014) and noted in other studies (Leighton & Acrivos 1986; Charru & Mouilleron-Arnould 2002; Charru *et al.* 2016). This validates our approach for the problem in this study.

REFERENCES

- AKHAVAN, R., KAMM, R.D. & SHAPIRO, A.H. 1991a An investigation of transition to turbulence in bounded oscillatory Stokes flows. Part 1. Experiments. *J. Fluid Mech.* **225**, 395–422.
- AKHAVAN, R., KAMM, R.D. & SHAPIRO, A.H. 1991b An investigation of transition to turbulence in bounded oscillatory Stokes flows. Part 2. Numerical simulations. *J. Fluid Mech.* 225, 423–444.
- ANDERSON, T.B. & JACKSON, R. 1967 Fluid mechanical description of fluidized beds. Equations of motion. Ind. Engng Chem. Fundam. 6 (4), 527–539.
- APTE, S.V., MARTIN, M. & PATANKAR, N.A. 2009 A numerical method for fully resolved simulation (FRS) of rigid particle–flow interactions in complex flows. *J. Comput. Phys.* **228** (8), 2712–2738.
- AROLLA, S.K. & DESJARDINS, O. 2015 Transport modeling of sedimenting particles in a turbulent pipe flow using Euler–Lagrange large eddy simulation. *Intl J. Multiphase Flow* **75**, 1–11.
- AUSSILLOUS, P., CHAUCHAT, J., PAILHA, M., MÉDALE, M. & GUAZZELLI, É. 2013 Investigation of the mobile granular layer in bedload transport by laminar shearing flows. *J. Fluid Mech.* **736**, 594–615.
- BLONDEAUX, P. & SEMINARA, G. 1979 Transizione incipiente al fondo di un'onda di gravità. *Atti Accad. Naz. Lincei Classe di Scienze Fis. Matematiche e Naturali. Rend.* 67 (6), 408–417.
- BREUGEM, W.-P. 2012 A second-order accurate immersed boundary method for fully resolved simulations of particle-laden flows. J. Comput. Phys. 231 (13), 4469–4498.
- Breugem, W.P., Boersma, B.J. & UITTENBOGAARD, R.E. 2006 The influence of wall permeability on turbulent channel flow. *J. Fluid Mech.* **562**, 35.
- CAPECELATRO, J. & DESJARDINS, O. 2013a An Euler–Lagrange strategy for simulating particle-laden flows. J. Comput. Phys. 238, 1–31.
- CAPECELATRO, J. & DESJARDINS, O. 2013b Eulerian-Lagrangian modeling of turbulent liquid-solid slurries in horizontal pipes. *Intl J. Multiphase Flow* **55**, 64–79.
- CAPECELATRO, J., PEPIOT, P. & DESJARDINS, O. 2014 Numerical characterization and modeling of particle clustering in wall-bounded vertical risers. Chem. Engng J. 245, 295–310.
- CARSTENSEN, S., SUMER, B.M. & FREDSØE, J. 2010 Coherent structures in wave boundary layers. Part 1. Oscillatory motion. *J. Fluid Mech.* **646**, 169–206.
- CARSTENSEN, S., SUMER, B.M. & FREDSØE, J. 2012 A note on turbulent spots over a rough bed in wave boundary layers. *Phys. Fluids* **24** (11), 115104.
- CHARRU, F., BOUTELOUP, J., BONOMETTI, T. & LACAZE, L. 2016 Sediment transport and bedforms: a numerical study of two-phase viscous shear flow. *Meccanica* **51** (12), 3055–3065.
- CHARRU, F. & MOUILLERON-ARNOULD, H. 2002 Instability of a bed of particles sheared by a viscous flow. J. Fluid Mech. 452, 303–323.
- CONLEY, D.C. & INMAN, D.L. 1994 Ventilated oscillatory boundary layers. J. Fluid Mech. 273, 261–284.
- COSTAMAGNA, P., VITTORI, G. & BLONDEAUX, P. 2003 Coherent structures in oscillatory boundary layers. J. Fluid Mech. 474, 1–33.
- DAVE, H. & KASBAOUI, M.H. 2023 Mechanisms of drag reduction by semidilute inertial particles in turbulent channel flow. *Phys. Rev. Fluids* **8** (8), 084305.
- FINN, J.R. & LI, M. 2016 Regimes of sediment–turbulence interaction and guidelines for simulating the multiphase bottom boundary layer. *Intl J. Multiphase Flow* **85**, 278–283.

- FINN, J.R., LI, M. & APTE, S.V. 2016 Particle based modelling and simulation of natural sand dynamics in the wave bottom boundary layer. *J. Fluid Mech.* **796**, 340–385.
- FYTANIDIS, D.K., GARCÍA, M.H. & FISCHER, P.F. 2021 Mean flow structure and velocity-bed shear stress maxima phase difference in smooth wall, transitionally turbulent oscillatory boundary layers: direct numerical simulations. *J. Fluid Mech.* **928**, A33.
- GHODKE, C.D. & APTE, S.V. 2016 DNS study of particle-bed-turbulence interactions in an oscillatory wall-bounded flow. J. Fluid Mech. 792, 232–251.
- GHODKE, C.D. & APTE, S.V. 2018 Roughness effects on the second-order turbulence statistics in oscillatory flows. Comput. Fluids 162, 160–170.
- GIBILARO, L.G., GALLUCCI, K., DI FELICE, R. & PAGLIAI, P. 2007 On the apparent viscosity of a fluidized bed. *Chem. Engng Sci.* 62 (1), 294–300.
- HAUSMANN, M., CHÉRON, V., EVRARD, F. & VAN WACHEM, B. 2024 Study and derivation of closures in the volume-filtered framework for particle-laden flows. *J. Fluid Mech.* **996**, A41.
- HINO, M., SAWAMOTO, M. & TAKASU, S. 1976 Experiments on transition to turbulence in an oscillatory pipe flow. J. Fluid Mech. 75 (2), 193–207.
- HSU, T.-J., JENKINS, J.T. & LIU, P.L.F. 2004 On two-phase sediment transport: sheet flow of massive particles. *Proc. R. Soc. Lond. A* 460, 2223–2250.
- JENSEN, B.L., SUMER, B.M. & FREDSØE, J. 1989 Turbulent oscillatory boundary layers at high Reynolds numbers. J. Fluid Mech. 206, 265–297.
- JEWEL, A., FUJISAWA, K. & MURAKAMI, A. 2019 Effect of seepage flow on incipient motion of sand particles in a bed subjected to surface flow. J. Hydrol. 579, 124178.
- KASBAOUI, M.H. 2019 Turbulence modulation by settling inertial aerosols in Eulerian–Eulerian and Eulerian–Lagrangian simulations of homogeneously sheared turbulence. *Phys. Rev. Fluids* **4** (12), 124308.
- KASBAOUI, M.H. & HERRMANN, M. 2025 A high-fidelity methodology for particle-resolved direct numerical simulations. Intl J. Multiphase Flow 187, 105175.
- KASBAOUI, M.H., KOCH, D.L. & DESJARDINS, O. 2019 Clustering in Euler–Euler and Euler–Lagrange simulations of unbounded homogeneous particle-laden shear. *J. Fluid Mech.* **859**, 174–203.
- KEMPE, T. & FRÖHLICH, J. 2012 An improved immersed boundary method with direct forcing for the simulation of particle laden flows. *J. Comput. Phys.* 231 (9), 3663–3684.
- KIDANEMARIAM, A.G. & UHLMANN, M. 2014 Interface-resolved direct numerical simulation of the erosion of a sediment bed sheared by laminar channel flow. *Intl J. Multiphase Flow* **67**, 174–188.
- LEIGHTON, D. & ACRIVOS, A. 1986 Viscous resuspension. Chem. Engng Sci. 41 (6), 1377–1384.
- LIU, P.L.-F., DAVIS, M.H. & DOWNING, S. 1996 Wave-induced boundary layer flows above and in a permeable bed. *J. Fluid Mech.* 325, 195–218.
- MAXEY, M.R. & RILEY, J.J. 1983 Equation of motion for a small rigid sphere in a nonuniform flow. *Phys. Fluids* **26** (4), 883–889.
- MAZZUOLI, M., BLONDEAUX, P., VITTORI, G., UHLMANN, M., SIMEONOV, J. & CALANTONI, J. 2020 Interface-resolved direct numerical simulations of sediment transport in a turbulent oscillatory boundary layer. J. Fluid Mech. 885, A28.
- MAZZUOLI, M., KIDANEMARIAM, A.G., BLONDEAUX, P., VITTORI, G. & UHLMANN, M. 2016 On the formation of sediment chains in an oscillatory boundary layer. *J. Fluid Mech.* **789**, 461–480.
- MAZZUOLI, M., KIDANEMARIAM, A.G. & UHLMANN, M. 2019 Direct numerical simulations of ripples in an oscillatory flow. *J. Fluid Mech.* **863**, 572–600.
- MAZZUOLI, M. & VITTORI, G. 2019 Turbulent spots in an oscillatory flow over a rough wall. *Eur. J. Mech. B/Fluids* **78**, 161–168.
- MEZA-VALLE, C. & PUJARA, N. 2022 Flow in oscillatory boundary layers over permeable beds. *Phys. Fluids* **34** (9), 092112.
- O'DONOGHUE, T. & WRIGHT, S. 2004 Flow tunnel measurements of velocities and sand flux in oscillatory sheet flow for well-sorted and graded sands. *Coast. Engng* **51** (11), 1163–1184.
- OZDEMIR, C., HSU, T.J. & BALACHANDAR, S. 2014 Direct numerical simulations of transition and turbulence in smooth-walled Stokes boundary layer. *Phys. Fluids* **26**, 045108.
- PEDOCCHI, F., CANTERO, M.I. & GARCÍA, M.H. 2011 Turbulent kinetic energy balance of an oscillatory boundary layer in the transition to the fully turbulent regime. *J. Turbul.* 12, N32.
- RAO, A.A. & CAPECELATRO, J. 2019 Coarse-grained modeling of sheared granular beds. Intl J. Multiphase Flow 114, 258–267.
- SAFFMAN, P.G. 1965 The lift on a small sphere in a slow shear flow. J. Fluid Mech. 22 (2), 385-400.
- SALON, S., ARMENIO, V. & CRISE, A. 2007 A numerical investigation of the Stokes boundary layer in the turbulent regime. J. Fluid Mech. 570, 253–296.
- SARPKAYA, T. 1993 Coherent structures in oscillatory boundary layers. J. Fluid Mech. 253, 105-140.

J.S. Van Doren and M.H. Kasbaoui

- Scott, G.D. & Kilgour, D.M. 1969 The density of random close packing of spheres. J. Phys. D: Appl. Phys. 2 (6), 863–866.
- SHUAI, S., DHAS, D.J., ROY, A. & KASBAOUI, M.H. 2022 Instability of a dusty vortex. J. Fluid Mech. 948, A56.
- SHUAI, S. & KASBAOUI, M.H. 2022 Accelerated decay of a Lamb-Oseen vortex tube laden with inertial particles in Eulerian-Lagrangian simulations. *J. Fluid Mech.* **936**, A8.
- SHUAI, S., ROY, A. & KASBAOUI, M.H. 2024 The merger of co-rotating vortices in dusty flows. *J. Fluid Mech.* 981, A27.
- SPARROW, K., POKRAJAC, D. & van der A, D.A. 2012 The effect of bed permeability on oscillatory boundary layer flow. *Coast. Engng Proc.* 1 (33), 26.
- STOKES, G.G. 1855 On the effects of internal friction of fluids on the motion of pendulums. *Trans. Camb. Phil. Soc.* 9, 197–229.
- TENNETI, S., GARG, R. & SUBRAMANIAM, S. 2011 Drag law for monodisperse gas—solid systems using particle-resolved direct numerical simulation of flow past fixed assemblies of spheres. *Intl J. Multiphase Flow* 37 (9), 1072–1092.
- UHLMANN, M. 2005 An immersed boundary method with direct forcing for the simulation of particulate flows. J. Comput. Phys. 209 (2), 448–476.
- VAN DOREN, J.S. & KASBAOUI, M.H. 2024 Turbulence modulation in dense liquid–solid channel flow. *Phys. Rev. Fluids* 9 (6), 064306.
- VITTORI, G., BLONDEAUX, P., MAZZUOLI, M., SIMEONOV, J. & CALANTONI, J. 2020 Sediment transport under oscillatory flows. *Intl J. Multiphase Flow* 133, 103454.
- VITTORI, G. & VERZICCO, R. 1998 Direct simulation of transition in an oscillatory boundary layer. *J. Fluid Mech.* 371, 207–232.
- VOERMANS, J.J., GHISALBERTI, M. & IVEY, G.N. 2017 The variation of flow and turbulence across the sediment–water interface. *J. Fluid Mech.* **824**, 413–437.
- XIONG, C., QI, X., GAO, A., XU, H., REN, C. & CHENG, L. 2020 The bypass transition mechanism of the Stokes boundary layer in the intermittently turbulent regime. *J. Fluid Mech.* **896**, A4.
- YUAN, J. & MADSEN, O.S. 2014 Experimental study of turbulent oscillatory boundary layers in an oscillating water tunnel. Coast. Engng 89, 63–84.